Published: 26 August 2025

Exploring the Adaptability of the Charge Transport Layers for Enhanced Efficiency in Lead-Free CH₃NH₃SnI₃ Perovskite Solar Cells

Md. Ibrahim Al Imran ^{1*}, Safia Aktar Dipa ^{2*}, Md. Shariful Islam Sharif ³, Molla Asif Zaman ⁴, and Abdullah Tanzib Mahdy ⁵

¹ University of Dhaka, Department of Biomedical Physics and Technology, Dhaka, Bangladesh

^{2*,3,4,5}Gopalganj Science and Technology University, Department of Electrical and Electronic Engineering, Gopalganja, Dhaka, Bangladesh

imran.bmpt@du.ac.bd, dipa.eee@gstu.edu.bd, mdsisharif603@gmail.com, asifzamanbg@gmail.com, tanzibmahdy2050@gmail.com

Abstract

Perovskite solar cells (PSCs) have attracted a lot of interest due to their remarkable energy transformation productivity (PCE) and the possibility of their application in both organic and inorganic compounds. Perfect for sustainable solar technologies, methylammonium tin iodide (CH₃NH₃) is a lead-free, non-hazardous perovskite displaying amazing optoelectronic properties. Its tunable bandgap helps to absorb solar energy efficiently. Its cost and great efficiency render it a perfect photovoltaic material. To improve essential characteristics of the hole transport layer (HTL), absorption area, and electron transport layer (ETL), this work models CH₃NH₃SnI₃-based PSCs using SCAPS-1D software. Simulations have been used to investigate the utility of CH₃NH₃SnI₃-based PSCs using Cu₂O as the HTL and including WS₂, C₆₀, IGZO, and ZnO as ETL compounds. Moreover, the effects on essential performance criteria like power fill factor (FF), conversion efficiency (PCE), open-circuit voltage (V_{0c}), and short-circuit current density (J_{5c}) of thickness, defect levels, absorber, HTL, and ETL have been investigated. The results show how much changing the ETL improves device efficiency. With PCE values of 33.43%, 33.19%, 33.19%, and 33.23%, respectively, ETLs consisting of WS₂, C₆₀, IGZO, and ZnO have been shown. Furthermore, this work investigated the effect of temperature on PSC performance. These results demonstrate quantum efficiency (QE) and the current density-voltage (J-V) responses.

Index-words: Perovskite Solar Cell (PSC), Lead-free, $CH_3NH_3SnI_3$, SCAPS-1D, ETL, HTL, WS_2 , C_{60} , IGZO, ZnO.

I. Introduction

Energy has become an essential requirement in nearly all aspects of contemporary life. By 2026, over one-third of the global energy is expected to derive from renewable sources, supporting climate objectives and reducing greenhouse gas emissions [1]. Due to its abundant availability and ease of use for efficient energy conversion compared to alternative sources of energy, solar power is regarded as one of the most promising alternatives [2].

A photovoltaic solar cell, commonly referred to as a solar cell, is a solid-state device that utilizes an electrical system (p-n junction) to directly transform sunlight into direct current (DC) through the photovoltaic effect. The discoveries related to the photovoltaic effect have led to the evolution

of modern solar technology and solar cells. Developments in manufacturing technologies and materials have lowered the cost of solar panels, therefore enabling solar electricity to be more reasonably priced and widely available.

A. Basic PV parameters

The performance and behavior of photovoltaic cells are detected by parameters, open-circuit voltage (V_{oc}) , short current (J_{sc}) , fill factor (FF), and efficiency of power conversion (PCE).

1. Open Circuit Voltage (V_{oc}) is the peak output voltage that the solar cell can generate when its terminals are unconnected, indicating that no current flows.

$$V_{oc} = \left(\frac{\alpha KT}{q}\right) ln \left(\frac{I_L}{I_0}\right) \tag{1}[3]$$



 α represents the optimum factor; K denotes the Boltzmann constant, roughly 1.38×10^{-23} J/K; I_0 and I_L are the dark saturation and lightgenerated current, respectively. T is the temperature in Kelvin; q is the elementary charge.

2. Short Circuit Current Density (J_{sc}) is the maximum current generated by that cell while the connectors of a solar cell are connected directly.

$$J_{sc} = \frac{I_{sc}}{\Delta} \tag{2}$$

Where A is the area of the solar cell.

3. Fill Factor (FF) is found by scaling the maximum power that is accessible (P_{max}) by the outcome of the voltage of an open circuit (V_{oc}) and the current density of a short circuit (I_{sc}).

$$FF = \frac{P_{max}}{J_{sc} \times V_{oc}} \tag{3}$$

4. Power Conversion Efficiency (PCF) is the percentage of the highest possible power. The ratio of the greatest power generated, P_{max} , to the power incoming, P_{min} , is represented by η .

$$\eta = \frac{P_{max}}{P_{min}} \tag{4}$$

B. Solar cell's working principle

Solar technology captures sunlight through diminutive photovoltaic (PV) cells [3]. The functioning of a photovoltaic panel comprises three primary stages,

- 1. Light absorption produces electron-hole pairs.
- 2. An internal electrical field segregates these charge carriers.
- 3. The segregated carriers traverse into a different circuit.

When sunlight impinges on a solar cell, it energizes particles within the semiconductor, generating electron-hole pairs. The electrical field at the junction of p and n directs electrons towards an n-type layer and holes towards the p-type layer, thereby inhibiting recombination. This motion enables electrons to traverse an external circuit, producing direct current (DC) electrical power, which can

be utilized to energize devices. A photocurrent is generated during illumination. In the event of a circuit short, the outside current will match the photocurrent (I_{ph}) produced by the incoming light.

$$I_{sc} = -I_{ph} = KI \tag{5}$$

Where I represents the intensity of the incoming light, and K is a device-specific constant. The dark current is given by the usual forward-bias p-n junction diode equation,

(2)
$$I_{diode} = I_0 \left[e^{\frac{eV}{\sigma KT}} - 1 \right]$$
 (6)

Where σ is the diode ideality factor and e is the elementary charge. Hence, the total current through the illuminated solar cell will be,

$$I = I_{ph} + I_{diode} = -I_{ph} + I_0 \left[e^{\frac{eV}{\eta KT}} - 1 \right]$$
 (7)

This equation integrates the photocurrent that is generated and the diode current to denote the total current generated by the solar cell.

In this work, a numerical investigation of lead-free perovskite solar cells (PSCs) utilizing a device architecture comprising ITO/ETL (WS₂, C₆₀, IGZO, ZnO)/CH₃NH₃SnI₃/HTL (Cu₂O)/Au was developed. Indium Tin Oxide (ITO) is selected as the transparent conductive oxide (TCO) because of its superior optical transmittance, exceptional electrical conductivity, and enduring stability in solar energy sources [4].

Among the chosen electron-carrying layers (ETLs), tungsten disulfide (WS2) is regarded as a promising candidate due to its superior electrical conduction, substantial absorption coefficient (>10³ cm⁻¹), and appropriate band gap for effective charge transfer [5]. Likewise, fullerene (C60) serves as prevalent electron transport layer (ETL), characterized by high electron mobility, exceptional stability, and the capacity to effectively remove ions from the perovskite substrate [6]. ETL being evaluated is indium gallium zinc oxide (IGZO), recognized for its extremely high electron mobility, low defect density, and superior optical transparency, which enhances device performance [7]. Zinc oxide (ZnO) is utilized due to its extensive bandgap (~3.3 eV), economical manufacturing process, high electron-withdrawing capacity, and robust stability, rendering it a feasible alternative for electron transport layers (ETL) [6].

Methylammonium-tin-iodide (CH₃NH₃SnI₃) was selected as an absorber layer because it is environmentally friendly, lead-free, and has strong light absorption and excellent optoelectronic properties, which are essential for efficient solar energy conversion [8].

Copper (I) oxide (Cu₂O) was selected as the layer used for transporting holes (HTL) due to its wide bandgap (>3.5eV), great hole mobility, nontoxic characteristics, and exceptional stability, all of which are crucial for efficient hole extraction and transportation in the device being studied [9]. Ultimately, gold (Au) served as the rear metal contact, offering superior electrical conductivity, an advantageous work function, and robust connectivity, thereby improving charge collection performance and overall stability of the device [9].

The primary parameters of photovoltaic performance, including absorber thickness of layers, ETL and HTL substrate thickness, doped concentration, defect density, and the state of interface defects, are examined. The impact of temperature during operation on device performance was also evaluated. Essential performance metrics, such as current density-voltage (J-V) properties and quantum efficiency (QE), are methodically evaluated to determine the viability of the recommended solar cell design.

II. Background studies

A. Perovskite Solar Cells (PSCs)

PV solar cells have attracted significant attention best efficient third-generation solar technology due to their high absorption coefficient, with improved carrier transport, simple fabrication process, and band gap tuning capability [10]. The power conversion efficiency (PCE) of the first PSCs in the laboratory in 2009 was about 3.8%, which has increased significantly to reach about 25.8% in 2020 [10].

This quick development of the PSCs has been made possible mainly by advancements in material quality, which are achieved by improved synthesis techniques and a deeper understanding of the growth process of metal halide perovskites (MHP). These insights into the complex and interrelated processes in perovskite growth are important for the development of high-efficiency growth strategies.

Element structures to PSC denoted ABX_3 , which was first proposed by Mitzi in 1990 [11]. Here, A is referred to as an organic cation, for example, (MA⁺, CH₃-NH₃⁺), and some inorganic cations like cesium Cs. The B is denoted by the metal ions like Sn²⁺or Ge²⁺, and X denotes halide ions, including I⁻, Cl⁻, or Br⁻[12].

 $BaZrS_3$ -based perovskite cell achieves an efficiency of 26.53% [13], within the introduction of titanium alloy, it improves up to 28.6% [13]. Shimul et.al presented a lead-free FTO/TiO2/Ca3AsCl3/CBTS/Ni structure with PCE of 23.70% [14].

B. CH₃NH₃SnI₃-based PSCs

Different studies have reported that the power conversion efficiencies (PCE) of lead (Pb)-based perovskites are generally higher than those of the lead-free perovskites [15]. However, due to their high efficiency, the Pb-based perovskites pose risks to nature and humans due to lead toxicity [16]. Consequently, researchers have concentrated on lead-free alternatives, among which (Sn)-based solar cells have emerged as promising candidates. Since tin belongs to Group 14 of the periodic table, like lead, it shares similar chemical properties and valence electron configurations. This similarity has driven research efforts to explore Sn-based perovskites as viable substitutes for Pb-based perovskites [17].

CH₃NH₃SnI₃ (MASnI₃), a well-known tin halide perovskite, has demonstrated remarkable potential as an absorber material for its small band gap (1.1–1.5 eV) and excellent charge transport properties [18]. Furthermore, Sn-based perovskites exhibit low extraction binding energy and higher carrier mobility [19]. The main problem in Sn²⁺ perovskites was their tendency to oxidize into Sn⁴⁺, leading to rapid degradation and severe device instability [20]. To mitigate this issue, SnCl₂ is often incorporated as an additive, and bromine (Br) doping has been explored to enhance stability and minimize Sn²⁺ oxidation [21].

MASnI₃ is considered a material that is synthesized using solution-processing techniques. Early research in 2014 demonstrated a PCE of 5.73% using MASnI₃ in planar heterojunction solar cells [22]. Later, inverted planar MASnI₃-based devices with better interfacial engineering achieved a higher efficiency of 7.14%, showing improved stability compared to traditional perovskite structures [23].

Another study achieved a breakthrough efficiency of 9.0% in MASnI₃-based solar cells by using a self-assembled monolayer (SAM) [24].

In addition to experimental advancements, theoretical simulations have been conducted to further optimize the characteristics of MASnI₃-based PSCs. A study anticipated that, through adjusting the doped level, defect density, and connection engineering, a power conversion efficiency (PCE) of 23.5% might be attained [25]. Additionally, mixedcation MASnI₃ structures have shown improved structural stability, with operational lifetimes exceeding 1000 hours under ambient conditions [25]. Recent studies exploring different solar structures, i.e., (CH3NH3)2CuCl4 [26], Glass/FTO/ WS2/CsSnI3/NiO, glass/FTO/ZnSe/CsSnBr3/CBTS/ Ni, and CsSnBr3 [27,28] have achieved better PCF and less toxic environmental impact.

Despite the progress, stability remains a significant challenge for tin-based perovskites. However, recent advances in surface passivation techniques and the development of low-dimensional MASnI₃ quantum dots have resulted in significant enhancements in both stability and productivity. For example, MASnI₃ PSC quantum dots, synthesized via a one-pot method, reached an efficiency of 10.32% and retained 85% of their starting performance over 90 days, thanks to the addition of antioxidant additives [29].

In another approach, MASnI₃ solar cells with hybrid 2D/3D perovskite structures achieved an even higher efficiency of 12.5%, and enhanced stability, as the 2D layer helped prevent tin oxidation and interfacial recombination [30]. Further research, including doping strategies with Ge, Bi, and Sb, has shown promising results, with efficiencies surpassing 14% in MASnI₃-based PSCs [31]. Moreover, advanced simulation studies suggest that with ideal charge transport layers, MASnI₃-based solar cells could reach a theoretical efficiency of 26.7%, indicating significant potential for future improvement [32].

III. Materials and methodology

A. Numerical simulation of SCAPS-1D

In the present work, the proposed structure's numerical model is analyzed via SCAPS-1D software (v 3.3.2.0), first introduced in 1998 [33-35]. This software can analyze photovoltaic performance

parameters such as J_{sc} and V_{oc} . FF, PCE by solving Poisson equations, the continuity of the equation for electrons or holes, the drift or diffusion equations, and the optical absorption coefficient equation. The equation of Poisson [34],

$$q - \frac{\partial y}{\partial x} \left[-\varepsilon(x) \frac{\partial V}{\partial x} \right] = q[p(x) - n(x) + N_D^+(x) - N_A^-(x) + p_t(x) - n_t(x)].$$
(8)

The equation of hole and electron continuity [35,36],

$$\frac{\partial P}{\partial t} = \frac{1}{q} \frac{\partial j_p}{\partial x} + G_p - R_p \tag{9}$$

$$\frac{\partial n}{\partial x} = \frac{1}{q} \frac{\partial j_p}{\partial x} + G_n - R_n \tag{10}$$

Here, q is the charge, v is the electric potential, and ε is the dielectric permittivity. Functions p(x) and n(x) denote concentrations of free electrons and holes, respectively, while $N_A^-(x)$ and $N_D^+(x)$ refer to densities of ionized donors and acceptors, respectively. The generation rates of holes and electrons are described by G_n and G_p . Furthermore, $p_t(x)$ and $n_t(x)$ represent trap densities for holes and electrons. Recombination rates to holes and electrons are labeled as R_n and R_p . Finally, the hole and electron current densities are represented by J_n and J_p . Drift and diffusion equations [37],

$$J_n = D_n \frac{dn}{dx} + \mu_n n \frac{d\varphi}{dx} \tag{11}$$

$$J_{p} = D_{p} \frac{dp}{dx} + \mu_{p} p \frac{d\varphi}{dx} \tag{12}$$

Here, D_p and D_n represent the diffusion coefficients for free holes as well as free electrons, whereas μ_n and μ_p denote the mobility of holes and electrons. The optical absorption coefficient equation [37],

$$\alpha(\lambda) = \left(A + \frac{B}{hv}\right) \sqrt{hv - E_g} \tag{13}$$

Here, the optical frequency is denoted by v, the bandgap by E_g , the Planck constant by h, the absorption coefficient by $\alpha(\lambda)$, and A and B are arbitrary constants. Under standard test conditions (Spectrum of AM1.5 solar 1000W/m³, 300 K) the cell FF and efficiency,

$$FF = \frac{J_{max} \times V_{max}}{J_{sc} \times V_{oc}} \tag{14}$$

$$\eta = \frac{J_{max} \times V_{max}}{P_{in}} \tag{15}$$

 J_{sc} denotes short circuit current density, V_{oc} represents open circuit voltage, P_{in} signifies incident power, while J_{max} and V_{max} indicate maximum current density and voltage, respectively.

B. Proposed PSC structure

The proposed ITO/ETL (WS2, C60, IGZO, ZnO)/CH3NH3SnI3/HTL (Cu2O)/Au device structure is depicted in Fig. 1, with its band diagram shown in Fig. 2. Simulations were conducted at 300K under an AM 1.5 G spectrum and power density of 1000 W/m².

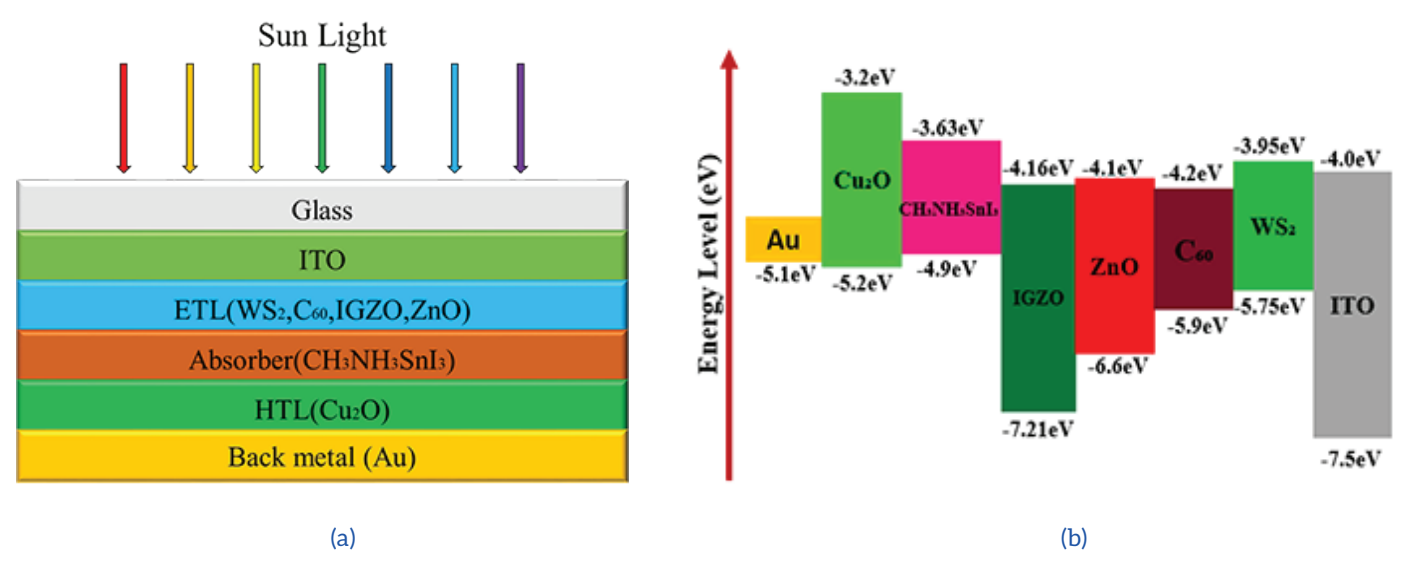


Figure 1: (a) Diagrammatic illustration of suggested PSC structure, and (b) Energy band alignment for constituent material.

Device and material parameters, sourced from summarized in Tables 1 and 2. theoretical models, experiments, and literature, are

Table 1: Input value of our simulation for different materials and layers

Parameters	ITO [37]	WS ₂ [38]	C60 [39]	IGZO [40,41]	ZnO [42]	CH3NH3SnI3 [43]	Cu ₂ O [44]
Thickness (µm)	0.1	0.4	0.03	0.03	0.05	1	0.1
Band gap (eV)	3.6	1.8	1.8	3.05	3.3	1.3	2.3
Electron affinity (eV)	4	3.90	3.9	4.16	4	4.2	3.4
Dielectric permittivity	9	13.6	4.2	10	9	10	7.5
CB effective DOS (cm ⁻³)	2.2×10 ¹⁸	2.2×10 ¹⁸	8.0×10 ¹⁹	5.0×10 ¹⁸	3.9×10 ¹⁸	2.2×10 ¹⁸	9.2×10 ¹⁹
VB effective DOS (cm ⁻³)	1.8×10 ¹⁹	1.8×10 ¹⁹	8.0×10 ¹⁹	5.0×10 ¹⁸	1.8×10 ¹⁹	1.8×10 ¹⁸	5.0×10 ²⁰
Electron mobility (cm²/Vs)	100	100	0.08	15	100	1.6	150
Hole mobility (cm²/Vs)	25	100	0.0035	0.1	25	1.6	100
Donor density N_D (cm ⁻³)	1.0×10 ¹⁹	1.0×10 ¹⁸	1.0×10 ¹⁹	1.0×10 ¹⁹	1.0×10 ¹⁹	0	0
Acceptor density N _A (cm ⁻³)	0	0	0	0	0	1.0×10 ¹⁸	1.0×10 ¹⁹
Defect density N_t (cm ⁻³)	1.0×10 ¹⁵	1.0×10 ¹⁵	1.0×10 ¹⁴	1.0×10 ¹⁵	1.0×10 ¹⁵	1.0×10 ¹⁴	1.0×10 ¹⁵

Table 2: Interface parameters [45]

Parameters	Cu ₂ O/CH ₃ NH ₃ SnI ₃	CH ₃ NH ₃ SnI ₃ /ETL	ETL/ITO
Defect type	neutral	neutral	neutral
capture cross section Electron (cm²)	1.0×10 ⁻¹⁹	1.0×10 ⁻¹⁹	1.0×10 ⁻¹⁹
capture cross section Hole (cm²)	1.0×10 ⁻¹⁹	1.0×10 ⁻¹⁹	1.0×10 ⁻¹⁹
Energetic distribution	Single	Gaussian	Single
Energy concerning reference	0.6	0.6	0.6
Characteristic Energy (eV)	-	0.1	-
Total density (cm ⁻²)	1.0×10 ¹³	1.0×10 ¹³	1.0×10 ¹¹

When sunlight falls on the CH₃NH₃SnI₃ layer, the perovskite material absorbs the photon. Once the energy of the photon exceeds the band gap of CH₃NH₃SnI₃, it excites electrons from the valence band (VB) to the conduction band (CB), resulting in the formation of electron-hole pairs [46]. These pairs must be separated and directed in opposite directions by an electric field at the p-n junction to generate electrical energy.

An external electric field propels the excited electrons through the conduction region of CH₃NH₃SnI₃ to the conduction band of the electron transportation layer (ETL). The ITO (indium tin oxide) front electrode is essential for collecting electrons from the absorber layer. The conductive band of the electron transport layer (ETL) is lower than that of CH₃NH₃SnI₃, facilitating an unobstructed pathway for electrons, hence ensuring an uninterrupted flow of electrons across the perovskite solar cell (PSC) [47]. Furthermore, the ETL mitigates electrical shunts between the absorber layer and transparent electrode [48]. The electrons are then gathered by the ITO electrode. Selecting the appropriate metal is crucial, since it guarantees efficient Ohmic connections, facilitates charge extraction, and minimizes Schottky barriers [49]. In this context, ITO, with a work function of 4.7 eV, facilitates this process.

During this time, Cu₂O's higher valence band (HTL) absorbs any remaining holes in the CH₃NH₃SnI₄ valence band. For efficient hole transfer, Cu₂O's high valence band acts as an energy barrier, blocking electrons from moving towards the anode [49]. After that, an electrode made of a rare metal is used to fill the holes. The metal electrode must be in alignment with the Fermi level of the valence band maximum (VBM) and conduction band minimum (CBM) of CH₃NH₃SnI₃ [50]. Gold (Au) is utilized as the back electrode (5.1 eV) to finish the circuit and connect

it to an external load. It collects the holes that have been transported from Cu₂O. The predictive modeling of PV solar cells for optimization, fault detection, and performance evaluation, the SCAPS-1D platform has been used extensively [50].

IV. Results and analysis

A. Band diagram of CH₃NH₃SnI₃

The amount of energy the material requires plays a crucial role in analyzing the performance of perovskite solar cells. In these cells, effective charge transfer is essential for holes to enter the hole transportation layer (HTL), while electrons must enter the conduction band, or BC, of the layer that carries electrons (ETL). The indium tin oxide and Au electrodes collaborate to gather holes and electrons. Ensuring an optimal balance of energy within the CH₃NH₃SnI₃ absorber and the ETL is crucial for facilitating efficient electron extraction. The electron affinity of the electron transport layers (WS₂, C₆₀, IGZO, and ZnO) must exceed that of the perovskite absorber layer (PAL). Conversely, for hole extraction at the CH₃NH₃SnI₃/Cu₂O interfaces, the ionization energy of Cu₂O must be inferior to the PAL. A discrepancy in the energy balances of these interfaces may adversely impact the photovoltaic performance of the devices.

The band diagrams of different device configurations ITO/WS₂/CH₃NH₃SnI₃/Cu₂O/Au, ITO/C₆₀/CH₃NH₃SnI₃/Cu₂O/Au, ITO/IGZO/CH₃NH₃SnI₃/Cu₂OAu, and ITO/ZnO/CH₃NH₃SnI₃/Cu₂O/Au are shown in Fig. 2. In thermal equilibrium, the Fermi level is unchanged throughout the whole device structure. When the devices are exposed to light, the photon-induced excitation disrupts this equilibrium, causing the formation of the Cu₂O Fermi level [51].

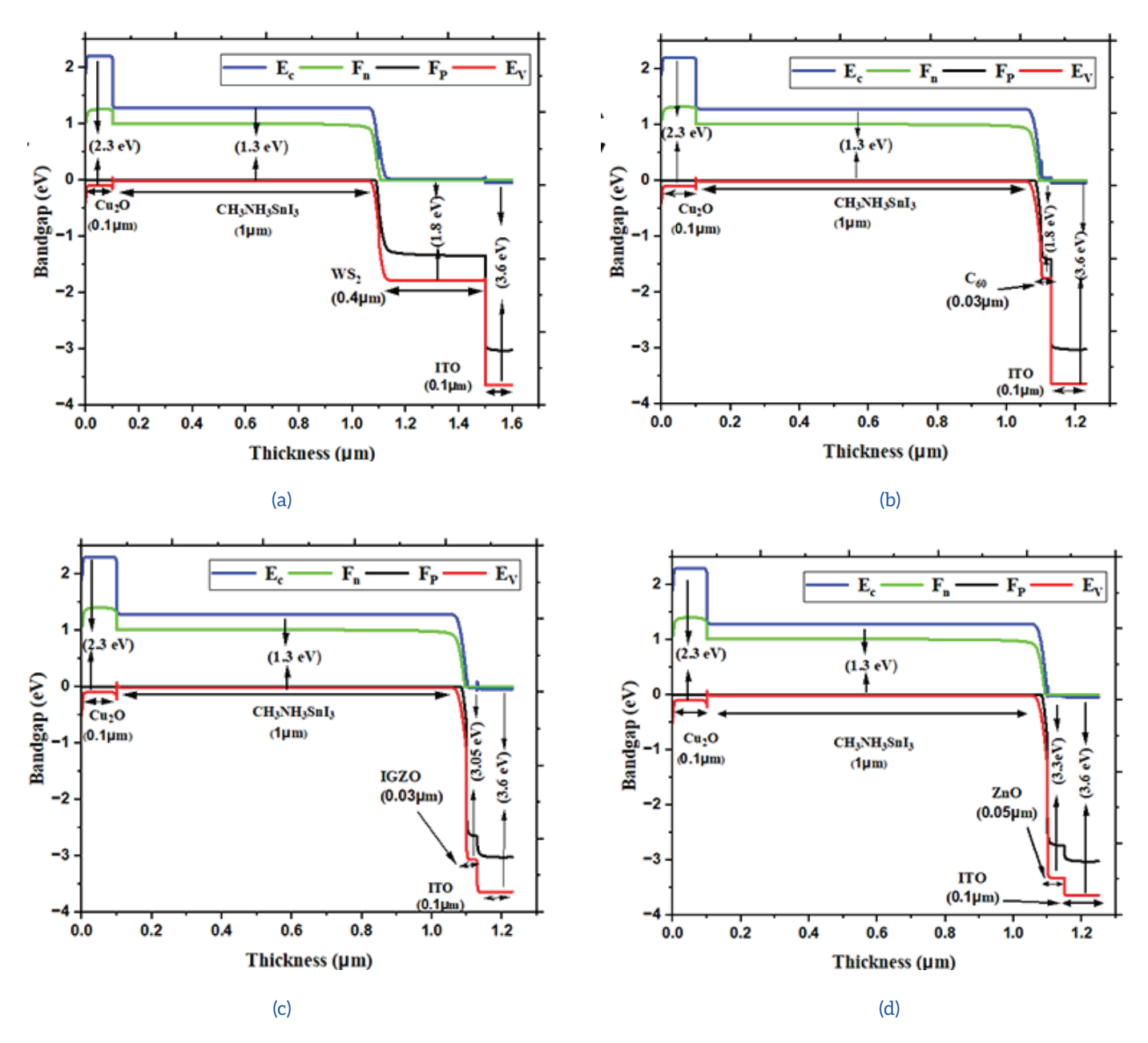


Figure 2: Energy band diagram for different ETL layers: (a) WS2, (b) C60, (c) IGZO, and (d) ZnO.

To facilitate efficient charge transfer, it is essential to optimize the band's valence offsets (VBO) at the $Cu_2O/CH_3NH_3SnI_3$ junction, as this will enhance hole mobility. Likewise, optimizing the conductive band offset (CBO) at the $CH_3NH_3SnI_3/ETL$ junction enhances the effective electron mobility. Ideally, the CBO negative facilitates efficient electron extraction and mitigates recombination, thereby enhancing the open circuit voltage (V_{oc}). Conversely, the negative valence band offset (VBO) among $CH_3NH_3SnI_3$ and the hole transport layer (HTL) facilitates hole extraction, thereby enhancing the short circuit current (I_{sc}) and the fill factor (FF).

However, if offsets are positive, then the energy

barriers may be created, which slow down the charge transfer and increase the recombination rate, resulting in a reduction in device output. So, energy balance optimization is very important, which ensures that charge separations occur effectively and energy dissipation is minimized. It is evident from the various figures that these optimized conditions help maintain high performance in every four device structures.

Furthermore, each energy band diagram reflects the effect of the built-in potential within the semiconductor material, as evidenced by the band twisting at the p-n junction. The built-in potential arises from the diffusion of charge carriers, resulting in a depletion region formed by the interaction of the p-type and n-type material. This energy barrier aids in regulating the rotation of charge carriers, thereby influencing the device's overall performance.

B. PV performance for absorber layer thickness and defect density

Augmenting a problem with frequency within a perovskite absorber surface can adversely affect material quality by elevating the carrier combination rate, potentially surpassing the transport production rate [51]. Consequently, minimizing defect density is essential for enhancing the performance of the absorber layer. Research has been conducted on the correlation between defect density and the thickness of CH₃NH₃SnI₃ absorbers, showing an effective connection between these two parameters. Optimizing defect density and absorber layer thickness can significantly enhance performance, contingent upon material quality and the structure of the device.

The dimension of the absorber layer is essential for light absorption and charge carrier generation. The primary objective is to ascertain an optimal thickness that will enhance light absorption and reduce recombination losses. Defects serve as recombination centers, directly impacting quantum efficiency, resulting in a reduction of the voltage of the open circuit (V_{oc}) along with fill factor (FF). The correlation between absorber layer dimension and defect density is highly intricate; increased thickness can enhance light absorption, yet it also generates more defects, thereby elevating recombination losses.

Consequently, to attain the highest level of power

conversion efficiency, it becomes imperative to optimize both the thickness of the absorber layer and the defect density. Achieving this balance requires a profound understanding of the properties of the material and processing techniques to ensure optimal results in light absorption and charge transfer.

Figs. 3 to 6 show the effect of defect density (N_t) and also absorber layer dimension, where photovoltaic properties such as V_{oc} , FF, J_{sc} , and PCE are analyzed.

Now, the value of N_t varies from 10^{11} cm⁻³ to 10^{18} cm⁻³, and the absorber layer dimension ranges from 0.4µm to 1.4µm. It can be seen in Fig. 3(a-d) that the Voc reduces significantly for WS₂, C₆₀, IGZO, and ZnO devices, from 1.206V to 0.774V, 1.216V to 0.744V, 1.202V to 0.734V, and 1.238V to 0.736V, respectively. Among the different configurations, the ITO/IGZO/CH₃NH₃SnI₃/Cu₂O/Au device showed the lowest dependence of N_t on V_{oc} . The devices using WS₂ exhibited the highest V_{oc} . When the value of N_t is below 10^{14} cm⁻³, the V_{oc} is almost unchanged and it depends very little on the dimension of the absorber layer.

This kind of behavior can be elucidated by the observation that when N_t is diminished, the impact of trap conditions is reduced. When N_t exceeds a specific threshold, trap-assisted recombination through the Shockley-Reed-Hall mechanism emerges predominantly. This leads to a diminished carrier lifetime and a reduced Cu₂O-Fermi level separation, resulting in a lower V_{oc} . Fig. 3(a-d) illustrates the V_{oc} trends for various ETLs, demonstrating a uniform behavior by the device topology.

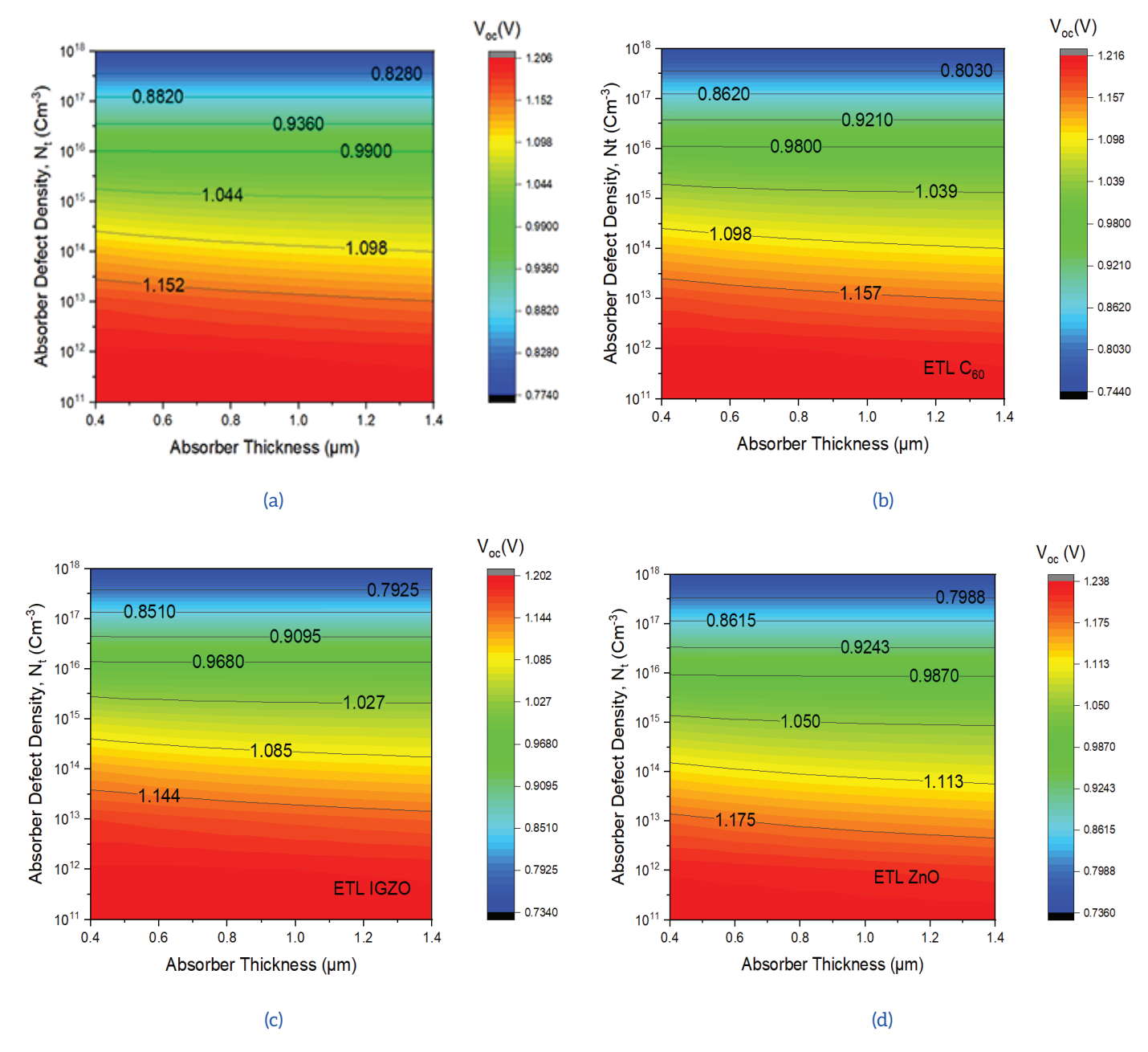


Figure 3: Open Circuit voltage for different ETL layers on the impact of absorber Thickness and defect density.

Fig. 4(a-d) shows that J_{sc} decreases from 35.25 mA/cm²to 19.45 mA/cm², from 35.30 mA/cm²to 11.70mA/cm², from 35.40 mA/cm² to 10.10 mA/cm², and from 35.40 mA/cm² to 35.49 mA/cm² to 10.40 mA/cm² for WS₂, C₆₀, IGZO, and ZnO devices, respectively. The ITO/IGZO/CH₃NH₃SnI₃/Cu₂O/Au configuration showed relatively little variation in J_{sc} . High

dependence was observed between devices using different ETLs, particularly when the thickness of the absorber layer was increased to more than 1μ m and N_t was below 10^{14} cm⁻³. Higher thickness can increase carrier generation and light absorption, but once the light penetration depth limit is exceeded, this effect becomes stable [52].

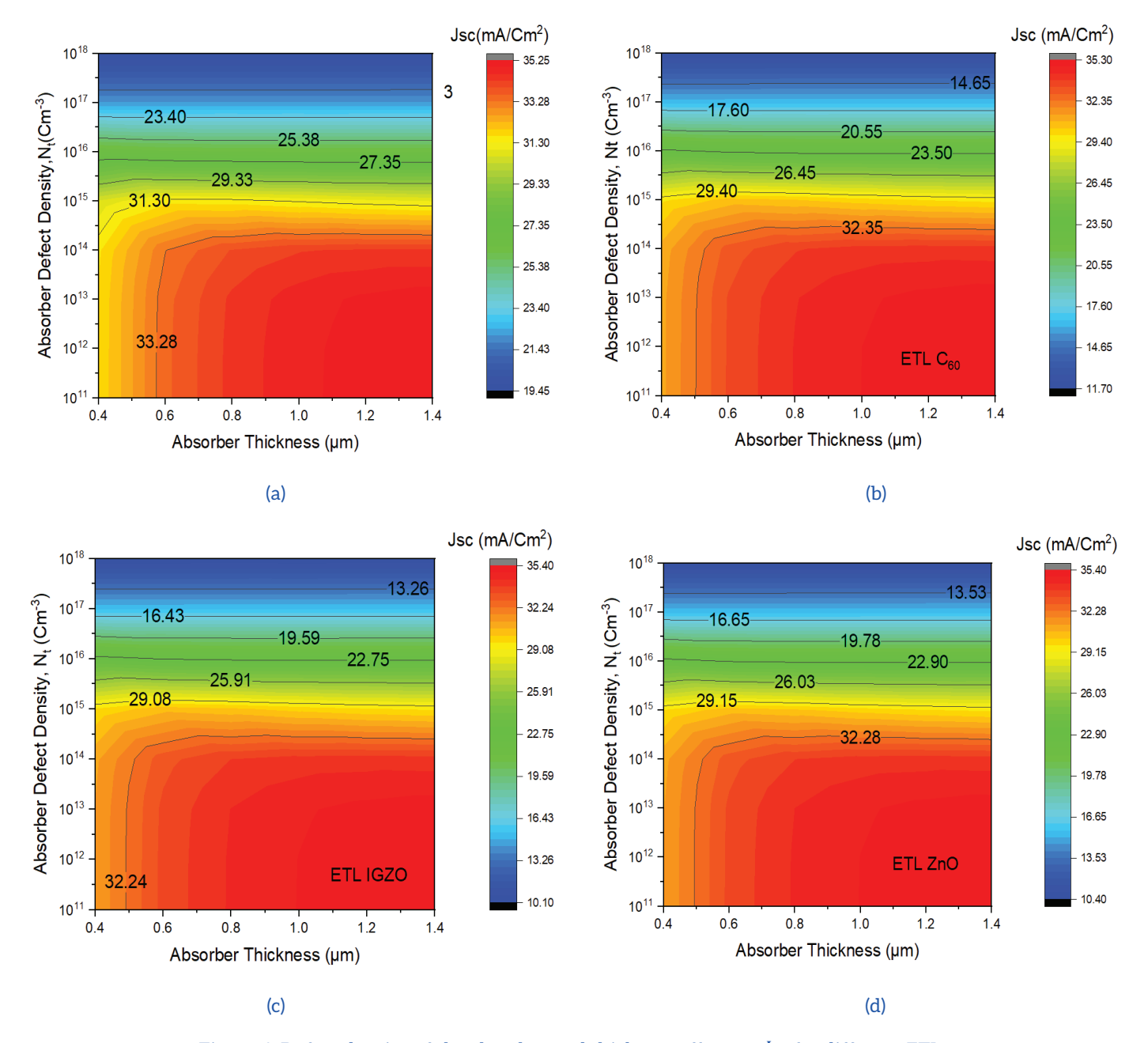


Figure 4: Defect density of the absorber and thickness effect on J_{sc} for different ETLs.

Fig. 5(a-d) shows that the FF decreased with increasing N_t . Specifically, the FF decreased from 89.20% to 74.90% for WS₂, from 89.80% to 68.00% for C₆₀, from 89.20% to 64.70% for IGZO, and from 89.90% to 65.10% for ZnO. Among all the configurations, the ITO/IGZO/CH₃NH₃SnI₃/Cu₂O/Au device showed the lowest change in FF. This behavior is closely related to V_{oc} , as FF is dependent on the recombination rate, which occurs in the depletion region [52]. When N_t is low, recombination is low, and FF remains stable,

allowing efficient charge collection. However, when N_t goes above a certain level, trap-assisted recombination significantly reduces the carrier collection efficiency, which causes a decrease in FF. Fig. 6(a-d) shows that.

The power conversion efficiency (PCE) of WS₂, C₆₀, IGZO, and ZnO devices diminished markedly, from 37.90% to 11.30%, from 38.50% to 5.9%, from 37.80% to 4.8%, and from 39.20% to 4.9%, respectively.

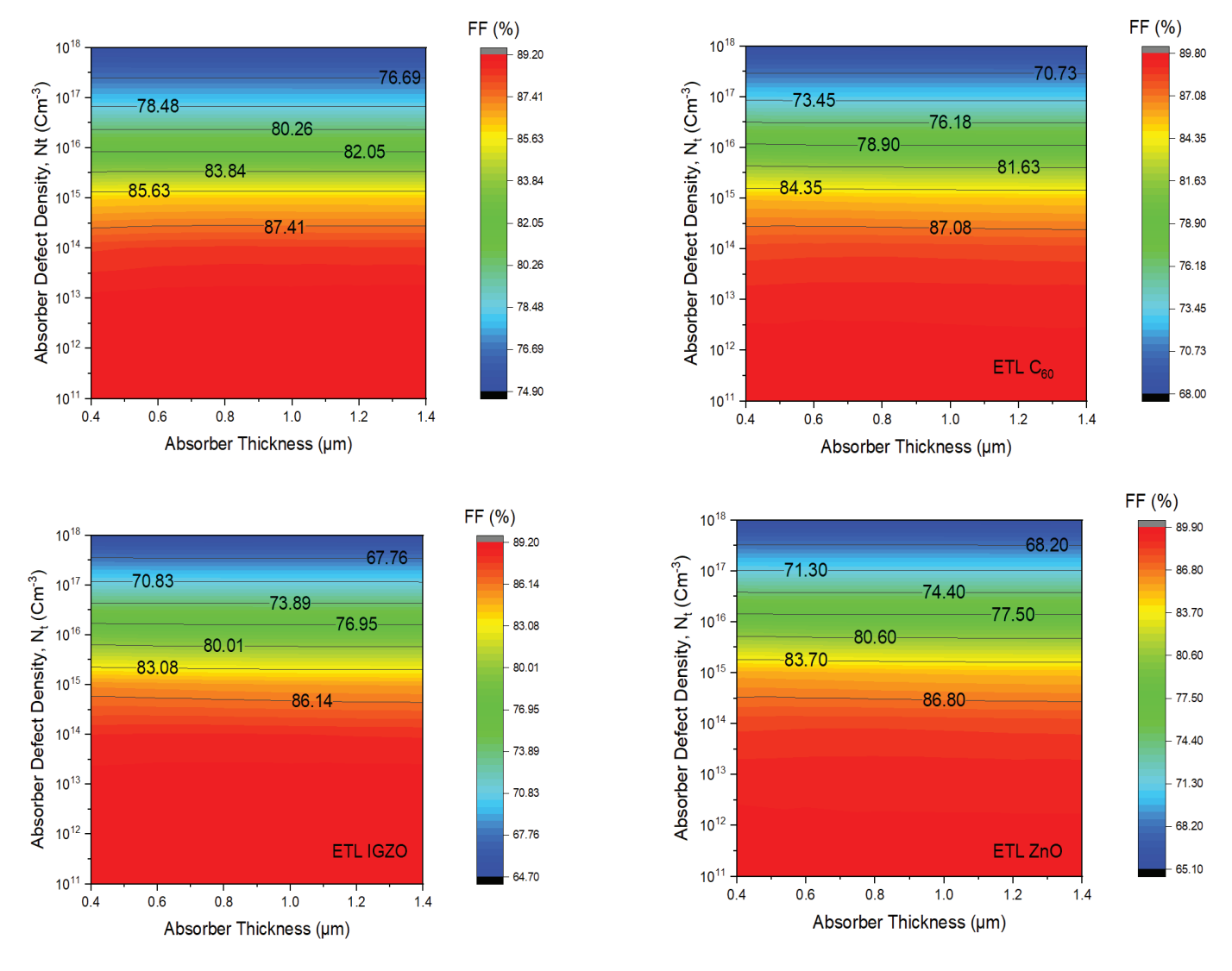


Figure 5: Absorber defect density and thickness effect on Fill Factor for different ETLs.

The efficiency of WS₂-based devices exceeded that of the others by approximately 1.0%. The maximum PCE was attained while the absorber layer diameter exceeded 1 μ m and N_t was less than 10¹⁴ cm⁻³. An augmented absorber layer enhances charge carrier production and optimizes light absorption. Nonetheless, elevated N_t enhances the density of

trap states, thereby augmenting recombination, diminishing carrier lifetime, and decreasing efficiency [52]. Simulation results demonstrate that optimal conditions for attaining maximum efficiency consist of a 1 μ m thick absorber layer as well as a carrier concentration (N_t) of 10¹⁴ cm⁻³.

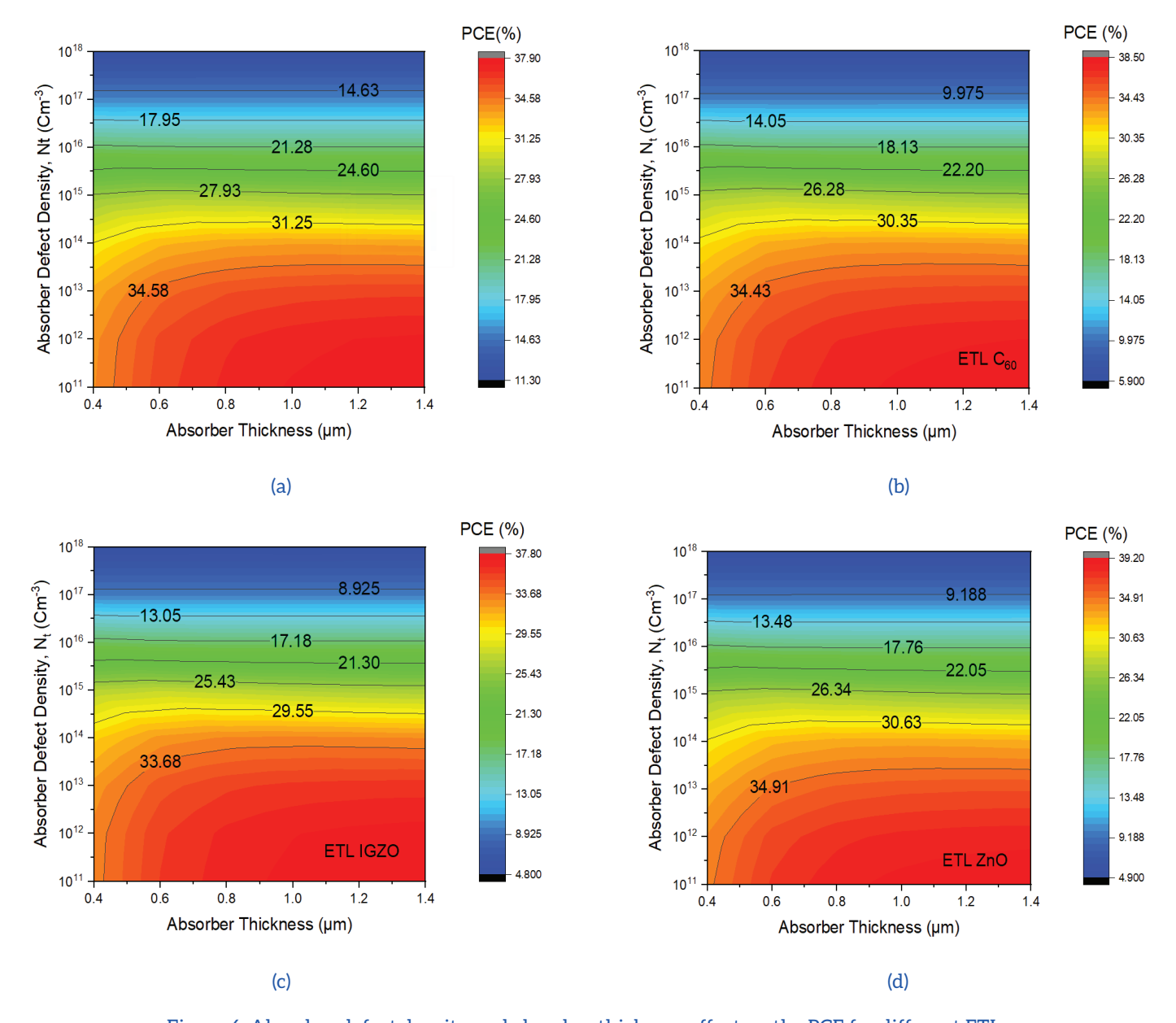


Figure 6: Absorber defect density and absorber thickness effect on the PCE for different ETLs.

C. Photovoltaic analysis of absorber layer N_D

Performance in devices with high acceptor doping density (N_A) is significantly improved [53]. Fig. 7 shows the impacts of variation N_A on the impact in devices with different electron transport levels (ETL), while it keeps the other acceptor, ETL, and hole transport level (HTL) parameters unchanged. This variation helps evaluate how the device's performances are affected and find the optimal doping level.

In the Electron transport layer-based structure, the open-circuit voltage is unchanged when it reaches N_A of 10¹⁵ cm⁻³. Next to this threshold, V_{oc} started to

increase as N_A was increased. This improvement in V_{oc} due to high doping concentrations is due to the lowering of the Fermi energy levels, which facilitates more efficient charge transfer [54]. Therefore, J_{sc} is equal to a maximum of 10^{15} cm⁻³, then it starts to decrease. Because of a decrease in J_{sc} , there is an improvement in the electron alloy in the absorber bulk, which becomes more pronounced with higher doping levels [54].

FF remains constant max. N_A 10¹⁴ cm⁻³, then FF started to increase with increasing N_A . However, in the case of WS₂-based structures, FF improved with increasing N_A up to 10¹⁷ cm⁻³. In particular, Efficiency improved significantly and increased N_A maximum 10¹⁷ cm⁻³ in most ETL configurations. However, in all

ETL-based devices, PCE decreased after N_A exceeded this ideal doping concentration. The primary cause for that efficiency decline is the formation of trap states resulting from elevated doping levels in the absorber layer, which impedes the mobility of charge carriers and elevates the reaction rate [55]. Additional doping changes the nature of the semiconductor, which can cause the perovskite material to behave as a metal, further reducing device performance. The ideal N_A of 10^{17} cm⁻³ was found for devices using Fig. 7.

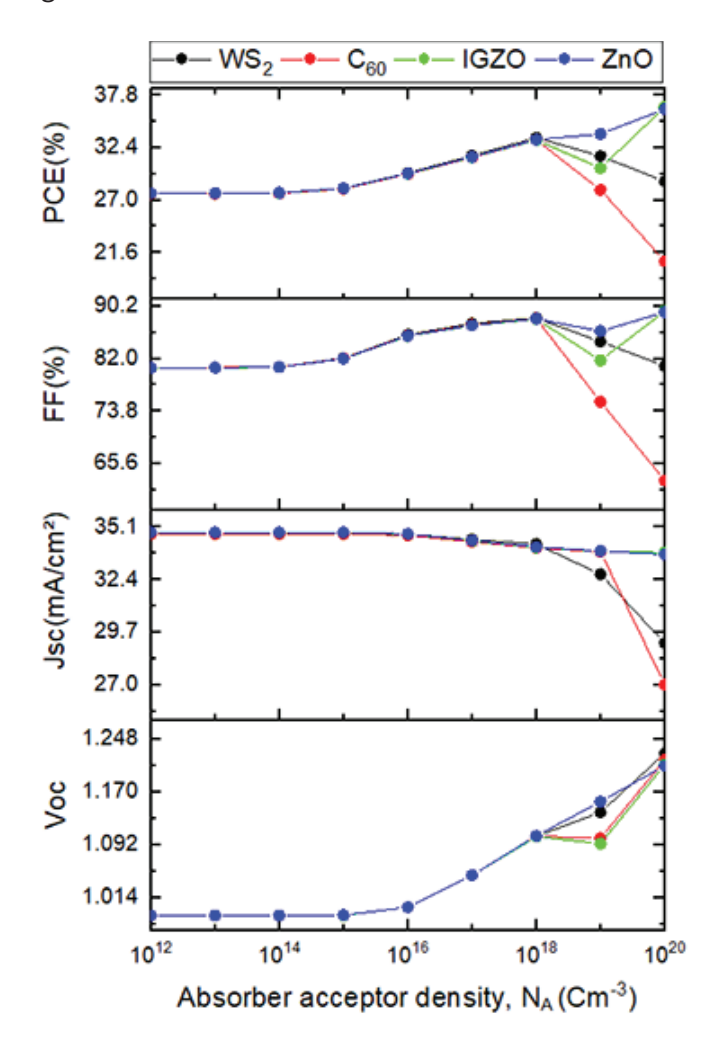


Figure 7: The plot of Absorber Acceptor density and 4 ETLs output parameters.

 C_{60} , ZnO, and IGZO-based ETLs. On the other hand, a higher N_A of 10^{18} cm⁻³ was identified as more suitable for future research for WS₂-based devices. The result shows that properly optimized N_A is important to improving structure performance, and further exploration of different ETL configurations is required to gain maximum results in terms of perovskite cell performance [55-57].

D. Electron Transport Layer thickness impact

The ETL thickness performs an essential function optimizing charge collection, decreasing recombination losses, and improving all efficiency on the device, which occurs by increasing the mobility of the electron [57]. The optimal ETL depth guarantees efficient ion separation, reduces resistance, and increases efficiency. An excessively thick ETL may result in inadequate ion prevention, hence augmenting interaction expenses at the junction. Conversely, too much ETL amplifies the resistance damage, causing a reduction of J_{sc} and FF. Consequently, it becomes crucial to accurately calibrate the ETL Thickness to achieve an optimal equilibrium between both the conductivity of electricity and optical accountability, thereby enhancing device efficiency.

Fig. 8(a) shows how changing the thickness from 0.1 to 0.6 μ m of the ETL affects the efficiency of the solar cell, while keeping other parameters the same. Results show that organic ETLs exhibit stability of performance over a wide thickness range. In particular, in the WS₂-based ETL structure, the PCE increased from 33.23% to 33.40% with increasing ETL thickness, along with increasing fill factor and short circuit current density, but V_{oc} is unchanged. These trends were made by the view of Sanger and Dar [58].

Besides, in fullerene-based ETL design, all the main parameters decreased with increasing thickness. Open circuit Voltage fell from 1.103 V to 1.087 V, but short circuit current density, fill factor, and Efficiency decreased from 32.27 mA/cm³ to 17.89 mA/cm³, from 88.17% to 87.93%, and from 31.39% to 17.11%, respectively. This negative trend for the C60-based ETL was reported [58]. Differences in Efficiency between devices fabricated on WS2, C60, IGZO, and ZnO are due to differences in electron mobility.

WS₂ and C₆₀ have high e-mobility, which increases efficiency, reduces loss of recombination, and improves efficiency. Moreover, surface roughness and pinholes in the electron transport layer can enhance recombination of electron-hole and hinder charge carriers, which ultimately reduces the efficiency of the perovskite [59].

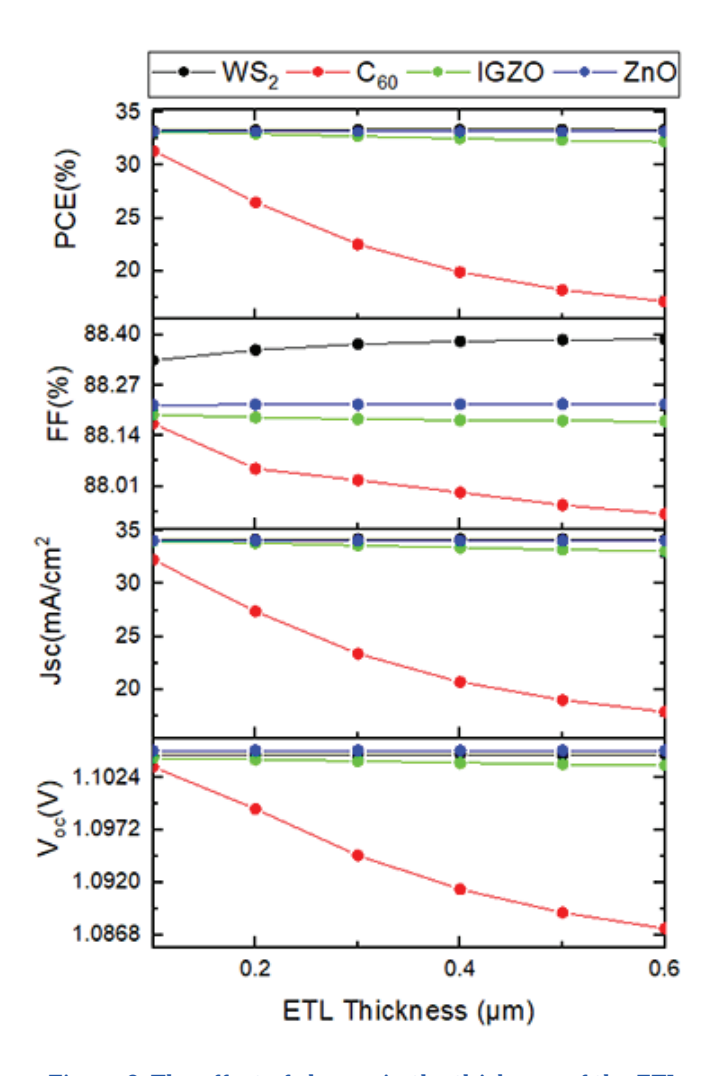


Figure 8: The effect of change in the thickness of the ETL layer on PV performance.

Ideal ETL thickness for WS₂, C_{60} , IGZO, and ZnO has been determined to be 0.4 μ m, 0.03 μ m, 0.03 μ m, and 0.05 μ m.

1. Analysis of the HTL interface

The optimization of charge collection for these functions—enhancing electron mobility, decreasing series resistance, lowering recombination expenses, and augmenting total system efficiency—is significantly influenced by the thickness of the electron transportation layer (ETL). The carefully selected ETL thickness ensures effective electron extraction while also reducing resistive losses and increasing power conversion efficiency. An insufficiently thick ETL may result in incomplete electron blocking, leading heightened recombination on the contact interface, whereas an overly thick ETL can induce resistive damages. consequently diminishing the density of the shortcircuit current (J_{sc}) and fill factor. Consequently, optimizing ETL thickness is crucial to achieve an

equilibrium between transparency in light and electrical conductivity, thereby enhancing device performance.

Fig. 8(a) presents the variation in efficiency of perovskite photovoltaic panels (PSCs) as the electron transport layer (ETL) thickness is altered from 0.1µm to 0.6µm, with all other parameters held constant. Inorganic electron transport layers, like ZnO and IGZO, have demonstrated consistent performance across various thicknesses. Specifically, in the WS₂based ETL configuration, the V_{oc} remained constant, whereas the PCE rose from 33.23% to 33.40% with the augmentation of ETL thickness. This enhancement was correlated with increased J_{sc} and FF, aligning with the findings of Dar and Sanger. Conversely, the C60-based ETL architecture exhibited a decline in critical parameters as thickness increased. Specifically, J_{sc} , FF, and PCE diminished from 32.27 mA/cm² to 17.89 mA/cm², from 88.17% to 87.93%, and from 31.39% to 17.11%, accordingly, while V_{oc} declined from 1.103 V to 1.087 V. This adverse trend was likewise noted by Otrokov et al. [60] for ETL as C60. The variations in PCE among devices utilizing WS₂, C₆₀, IGZO, and ZnO arise from disparities in electron mobility as well as energy band alignments within the CH₃NH₃SnI₃ absorber layer.

The enhanced electron mobility of WS₂ and C₆₀ promotes superior electron transport, leading to diminished recombination loss and increased power conversion efficiency (PCE). Conversely, IGZO and ZnO demonstrate low electron mobility and inadequate band alignment, impeding efficient electron extraction and transport, thereby leading to diminished PCE. Absence of this leads to surface defects and pinholes in the ETL layers, which promote recombination of electrons into holes, enhance series resistance, and impede charge transfer, ultimately diminishing solar cell efficiency.

The optimal ETL thicknesses are $0.4\mu m$ for WS₂, $0.03\mu m$ for C₆₀, $0.03\mu m$ for IGZO, and $0.05\mu m$ for ZnO. These values facilitate an optimal balance between electrical performance and material characteristics, thereby enhancing overall device efficiency.

E. PV Analysis of ETL donor density and HTL acceptor density

1. Analysis of ETL donor density

Fig. 9(a) illustrates the correlation between device efficiency and donor density (N_D) in an electron

transporting layer (ETL). The optimal donor density for maximizing device efficiency was progressively changed between 10^{15} cm⁻¹ to 10^{20} cm⁻¹ across various ETLs (WS₂, C₆₀, IGZO, as well as ZnO). The N_D of the ETL substantially influences the photovoltaic performance. Augmenting the N_D diminishes series resistance and enhances electron transport, thereby elevating energy conversion efficiency (PCE), voltage in the open circuit (V_{oc}), and fill factor (FF). Nonetheless, beyond a specific doping concentration, the power conversion efficiency (PCE)

and open-circuit voltage (V_{oc}) attain a saturation limit while charge transport and recombination stabilize.

Simulation outcomes for WS₂-based ETL indicate that an increase in N_D results in substantial enhancements across all critical performance metrics. V_{oc} raised within 1.105V to 1.125V, and FF enhanced from 71.82% to 88.22%. Despite a minor reduction in J_{sc} from 25.77 mA/cm² to 34.23 mA/cm², the PCE experienced a substantial increase from 20.82% to 33.43%.

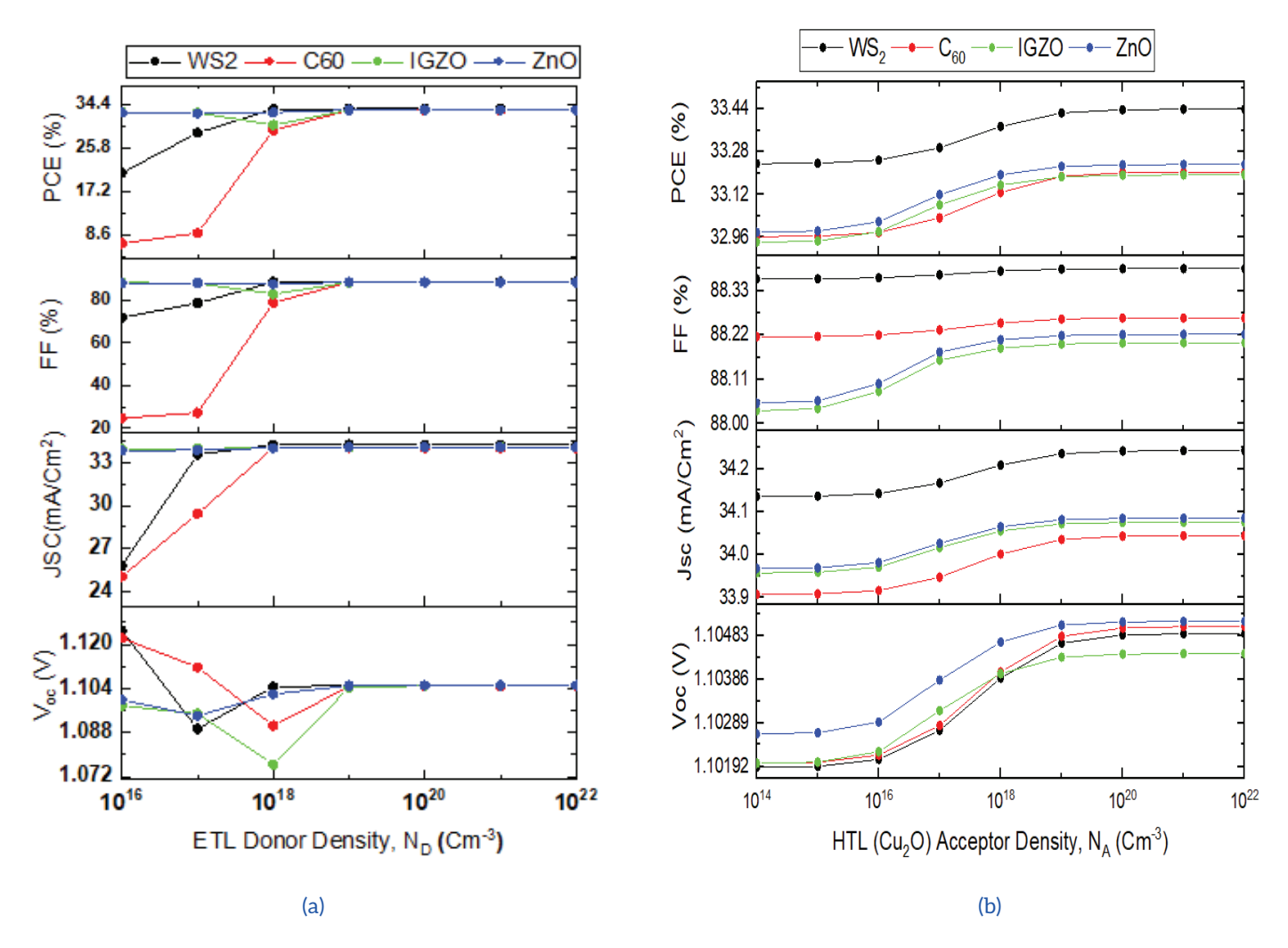


Figure 9: Effect of ETL donor density and HTL acceptor density for different parameters.

The enhancements, particularly at elevated donor densities, resulted from the augmented extraction of charges and efficiency of transport at the ETL-absorber junction [59].

Conversely, low N_D values diminish performance owing to heightened series resistance [59]. Except for the C_{60} -based structures, in which J_{sc} exhibited a slight decline as it increased donor density, other

devices utilizing ETL demonstrated analogous trends. The performance metrics of ETLs maximized upon attaining 10¹⁹ cm⁻¹, signifying that 10¹⁹ cm⁻¹ represents the optimal donor density across all ETLs.

2. Junction of HTL acceptor density

Fig. 9(b) depicts the effect of altering the accepted doping quantity (N_A) from 10^{14} cm⁻¹ to 10^{20} cm⁻¹, with all other parameters held constant. The

results indicate all of the metrics for performance demonstrate an increasing trend with the rise of N_A , stabilizing after attaining a specific value. The optimal amount of doping is determined as 10²⁰ cm⁻¹. Augmenting the acceptor level of doping in the Hole Transport Layer (HTL) material, Cu₂O, enhances hole extraction and diminishes recombination loss at the perovskite-HTL interface, leading to enhancements in power conversion efficiency (PCE), voltage at open circuits (V_{oc}), and short circuit current (I_{sc}). Among the evaluated ETL materials, WS₂ consistently showed superior performance owing to its advantageous band alignment and elevated electron mobility. Conversely, IGZO and ZnO demonstrated reduced efficiency for their less advantageous qualitative characteristics. These findings underscore the necessity of optimizing doping concentration to facilitate effective carrier separation and reduce power loss.

Elevating the doping intensity through enhanced resistivity of the HTL markedly enhances the PCE and current flow [60]. Consequently, an acceptor loading amount of 10²⁰cm⁻¹ for the HTL is identified as the optimal value to enhance device performance.

F. Analyzing the impact of interface defects on Photovoltaic Efficiency

1. Defect density effect on CH₃NH₃SnI₃/ETL interface

Fig. 10(a). examines the influence of the number of defects (N_t) on device performance along the CH₃NH₃SnI₃/ETL interface. The defect intensity is altered about 10¹⁰ to 10¹⁸ cm⁻³ to assess its impact. The rise in defect density leads to trap-assisted recombination, impeding the extraction of charge and diminishing carrier lifetime, resulting in a decline in the efficiency of power conversion (PCE), fill factor (FF), current in short circuits (J_{sc}), along with open circuit voltage (V_{oc}) as N_t increases at this interface.

Among the ETL materials, WS_2 demonstrated the highest defect tolerance owing to its optimal band alignment and minimal recombination rate, while C_{60} , as well as ZnO, were more prone to defects. In

all ETLs, the photovoltaic parameters remained relatively stable until N_t reached 10^{11} cm⁻³, beyond which a distinct performance decline was noted. Nonetheless, for C₆₀-based ETL, performance decline commences following a defect density of 10^{11} cm⁻³.

That decline in photovoltaic efficiency for the improvement on carrier generation and rate of recombination according to light penetration at the front of the device indicates the sensitivity of C_{60} to defects [60]. Therefore, the ideal defect density at the CH₃NH₃SnI₃/ETL interface for C_{60} -based ETL was determined to be 10^{11} cm⁻³, while the optimum N_t was found to be 10^{12} cm⁻³ for other ETL materials.

2. Defect density effect at Cu₂O/CH₃NH₃SnI₃ interaction

Fig. 10(b). Describe the effect of defect density on PV output at Cu₂O/CH₃NH₃SnI₃ interface. To evaluate how defect density affects key performance parameters, N_t is systematically changed between 10¹⁰ cm⁻³ and 10¹⁸ cm⁻³. Similarly, for the ETL interface, increasing N_t in $Cu_2O/CH_3NH_3SnI_3$ interaction leads to a drop in performance, accompanied by a substantial reduction in current through the short-circuit (J_{sc}) and voltage in the open circuit (V_{oc}) , indicating an increase in interfacial recombination losses. However, the impact on performance at Cu₂O/CH₃NH₃SnI₃ interaction is less severe than at the ETL interface, as the excellent conductivity and efficient hole extraction of Cu2O somewhat mitigate these losses.

The results show that, with increasing N_t at $\text{Cu}_2\text{O}/\text{CH}_3\text{NH}_3\text{SnI}_3$ junction, all output parameters deteriorate. Those performance parameters were relatively stable up to 10^{11} cm⁻³, after which a sharp efficiency decline was observed. This decrease in cell performance can be explained by the increase in resistance and the formation of trap states at the junction, which enhances recombination and degrades the entire device output [60].

Now, regardless of ETL material, the optimal defect density for Cu₂O/CH₃NH₃SnI₃ junction was found to be 10¹¹ cm⁻³.

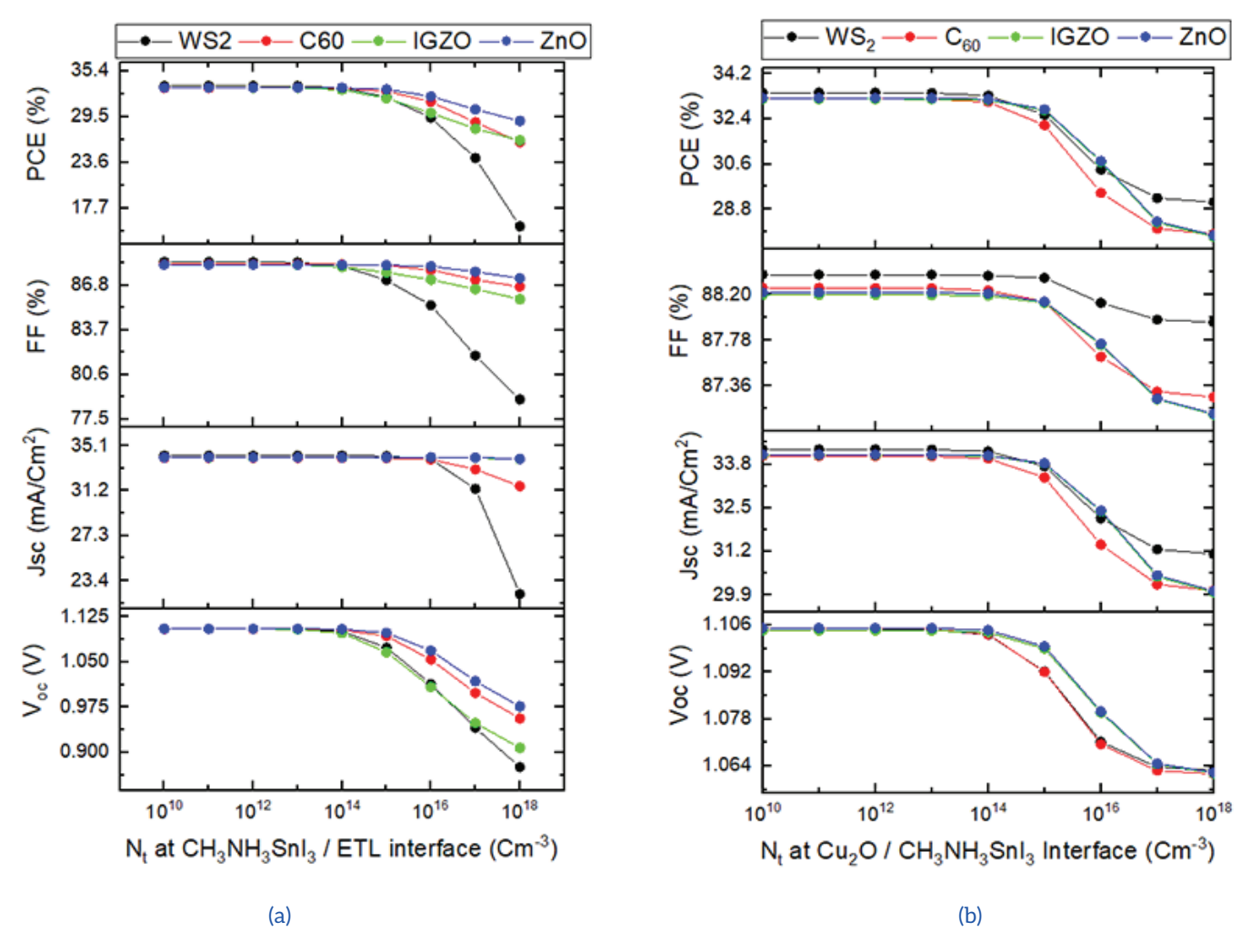


Figure 10: Effect of changing the defect density in the interface for (a) $CH_3NH_3SnI_3/ETL$, (b) $Cu_2O/CH_3NH_3SnI_3$ on solar performance.

G. Temperature effect on PV performance

There is a strong correlation between temperature and the stability of the operation of PSCs.

Table 3: Work function of different back contacts [60]

Metal	Ag	Fe	Au	Ni	Pb	Pt	Se
Work Function (eV)	4.74	4.81	5.1	5.5	5.6	5.7	5.9

Despite of exceptional efficiency and simplicity of preparation of PV solar cells (PSCs), substantial challenges persist in the large-scale manufacture of these gadgets. Stability and overall efficiency of PSCs are greatly influenced by outside variables, including UV radiation, ambient temperature, humidity, and moisture levels. Temperature is especially critical for these objects, as solar cells are frequently subjected to direct sunlight for extended durations, which can substantially elevate the temperature, occasionally reaching 45°C higher than ambient levels [61].

The semiconductor material of PSCs directly responds to the increase in temperature. While temperatures rise, the width of the material band diminishes due to the expansion of molecular spacing among the semiconductors. This phenomenon improves carrier mobility and electrical conductivity, thereby affecting the device's overall efficiency [62]. The standard operating temperature range for PSCs is from 275K to 500K, enabling researchers to systematically examine the effects of temperature fluctuations on device performance.

Fig. 11 offers an extensive examination of the influence of temperature on essential photovoltaic characteristics of perovskite solar cells (PSCs). The graph demonstrates that, across all device designs, the V_{oc} , FF, and PCE consistently diminish with rising temperature. In contrast, the (J_{sc}) stays comparatively stable and demonstrates negligible fluctuation with temperature. The decrease in V_{oc} is due to the opposite relationship with

saturated current density, and it rises with elevated temperature. The decline in PCE and FF is primarily attributed to increased series resistances, which hinder charge transfer at high temperatures, resulting in power dissipation and reduced device efficiency [62,63].

To support these observations, Gheno et al. [64] documented a similar trend in the behavior of PSCs with the increasing temperature. Their results further reinforce that the efficiency and durability of PSCs are greatly affected by the variation of photovoltaic parameters due to temperature.

Consequently, two important elements to ensure the large-scale viability of PSC technology are maintaining an ideal operating temperature and implementing effective thermal management strategies.

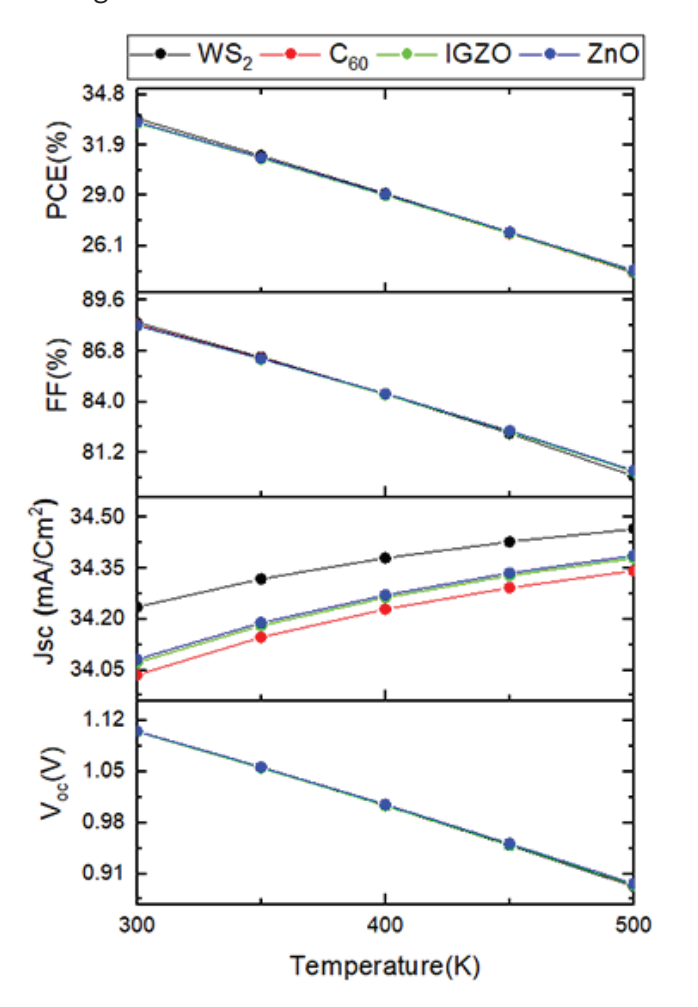


Figure 11: PV analysis on the temperature variation for different ETLs.

H. Analysis of the influence of J-V and QE characteristics

Both Fig. 12(a) and 12(b) show in detail the (J-V) and

(QE) characteristics of different (ETL) configurations of the ITO/ETL/CH₃NH₃SnI₃/Cu₂O/Au-based perovskite solar cell.

Among different ETLs, ITO/WS₂/CH₃NH₃SnI₃/Cu₂O/ Au structures produce the highest photocurrent, while the ITO/IGZO/CH3NH3SnI3/Cu2O/Au configuration provides the lowest photocurrent output. The improved photocurrent generation in the WS₂-based ETL is attributed to its high ability to enhance the charge transport, which highlights the important role of the band structure of ETL for the effective movement of photo-generated charge carriers on CH3NH3SnI3-based PSCs. This result is consistent with the previous studies, which confirms the importance of ETL properties for overall device performance. Notably, WS₂ produces the highest photocurrent but also achieves the highest (V_{oc}) , which significantly enhances the (PCE) of the device.

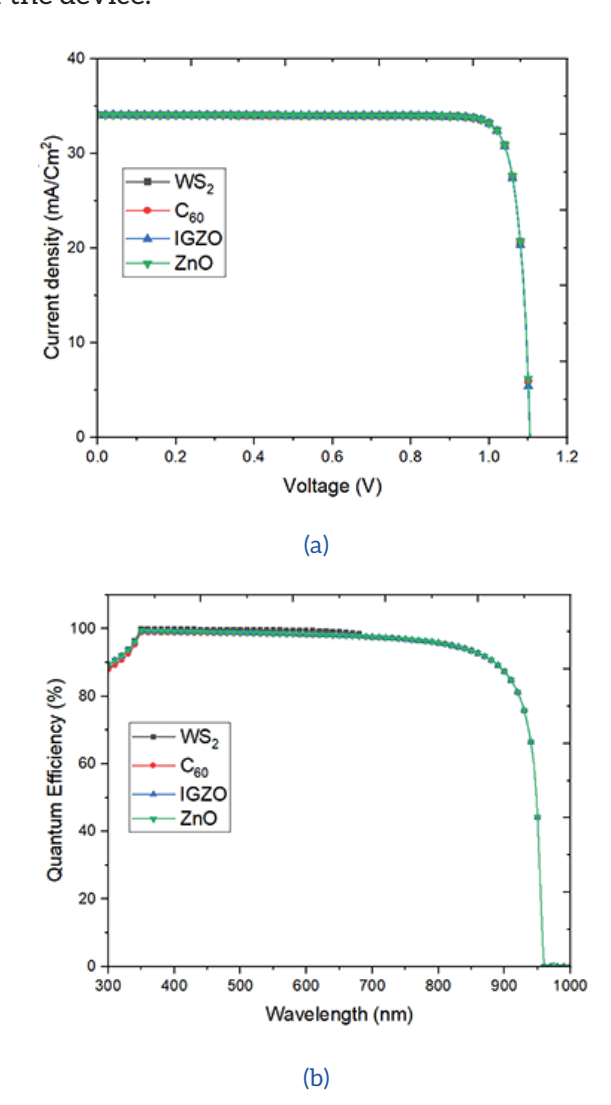


Figure 12: The influence of (a) J-V and (b) QE characteristic analyses on photovoltaic performance for various electron transport layers (ETLs).

Fig. 12(b). analyzes in more detail the relationship between (QE) and the wavelength (λ) of incident light, which lies in the range of 300-1000nm. According to the trend seen in the J-V curves, the ITO/C60/CH3NH3SnI3/Cu2O/Au structure shows the lowest QE value, while the ITO/WS₂/CH₃NH₃SnI₃/ Cu₂O/Au configuration achieves the highest QE. The QE of the WS₂-based device peaks at around 350nm, with a maximum value observed in the 350-550nm wavelength range, after which it starts to decrease. The decrease in QE above 600nm is mainly due to the low photon energy of long-wavelength light, which is unable to create effective hole-electron pairs. For this, absorption of photons and charge carrier production at long wavelengths become less efficient, which leads to a decrease in the overall device efficiency.

I. Final optimized result

In the proposed device architecture, multiple electron transport layer (ETL) elements are arranged in parallel, and Cu_2O is used as the hole transport layer (HTL). To improve the performance, various key parameters, such as doping concentration, defect density, layer thickness, and operating temperature, are systematically varied. Between the different Electron transport layer configurations, the WS₂-based ETL shows the highest performance, with a (V_{oc}) of 1.105 V, a (J_{sc}) of 34.24 mA/cm², a (FF) of 88.38%, and a (PCE) of 33.43%. The corresponding circuit of the design exhibiting the highest performance is shown in Fig. 13.

Table 4 represents a comparison of PV properties of every ETL-based perovskite cell with previous studies. Our results are in line with recent advances in perovskite solar cell (PSC) technology, particularly highlighting the potential for undoped and lead-free choices. By comparing

our simulation results with current research, we demonstrated the effectiveness and durability of our proposed design. This comparison is not only important in demonstrating the low toxicity of perovskite materials but also in demonstrating the effectiveness of our approach, which is capable of achieving efficiencies similar to those of traditional lead-based PSCs. These evaluations help to prepare a more disciplined roadmap for future development and identify areas that can be further improved and optimized. The theoretical foundation for the advancements of solar energy technology is solidified in our simulation results for the "ITO/ETL (WS₂, C₆₀, IGZO, and ZnO)/CH₃NH₃SnI₃/Cu₂O/Au" structures. Technical and economic hurdles must be surmounted to put simulation-based findings into real-world applications. Creating scalable, cost-effective manufacturing that doesn't sacrifice performance is the main challenge.

Ensuring the material's long-term stability against humidity, temperature variations, and UV exposure is also of utmost importance. To close the performance gap between theory and practice, future research will center on environmentally friendly materials and better encapsulation. Stable, high-performance perovskite solar cells will be used more frequently in next-generation photovoltaics as a result of these developments, which will increase their operational lifespan.

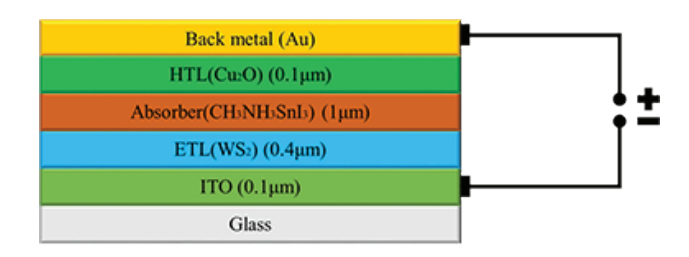


Figure 13: The proposed structure of maximum performance ITO/WS₂/ CH₃NH₃SnI₃/Cu₂O/Au

Table 4: Comparison of PV parameters of CH₃NH₃SnI₃-based PSC with previous literature

PV Cell structure	V_{oc} (V)	<i>J_{sc}</i> (mA/cm)	FF(%)	PCE(%)	Ref.
FTO/CdS/CH3NH3SnI3/Cu2O/Pt	0.878	33.40	85.25	25.02	[65]
Al/ZnO/SnO ₂ /CH ₃ NH ₃ SnI ₃ /Ni	0.961	34.63	84.63	28.19	[66]
FTO/TiO ₂ /CH ₃ NH ₃ SnI ₃ /Cu ₂ O/Pt	0.930	40.14	75.78	28.39	[67]
TCO/TiO ₂ /CH ₃ NH ₃ SnI ₃ /Cu ₂ O/Au	0.930	34.42	83.61	26.63	[68]
ITO/IGZO/CH3NH3SnI3/V2O5/Au	1.080	33.48	81.53	30.35	[69]
ITO/WS ₂ /CH ₃ NH ₃ SnI ₃ /Cu ₂ O/Au	1.104	34.23	88.38	33.43	Present Work
ITO/C60/CH3NH3SnI3/Cu2O/Au	1.104	34.03	88.26	33.19	Present Work
ITO/IGZO/CH3NH3SnI3/Cu2O/Au	1.104	34.07	88.20	33.19	Present Work
ITO/ZnO/CH3NH3SnI3/Cu2O/Au	1.105	34.08	88.22	33.23	Present Work

V. Conclusion

In this study, the SCAPS-1D simulation tool has been employed to design and analyze four novel configurations of lead-free perovskite solar cells, with a primary focus on the CH₃NH₃SnI₃-based absorber layer. A good architecture—comprising ITO/WS₂/CH₃NH₃SnI₃/Cu₂O/Au—was proposed and thoroughly investigated for its photovoltaic performance and material stability.

The results demonstrated that CH₃NH₃SnI₃, a tinbased perovskite, offers significant advantages as an environmentally friendly and non-toxic alternative to traditional lead-based perovskites. Through detailed simulations, we explored the impact of critical physical parameters, including absorber and transport layer thicknesses, interface defect densities, and doping concentrations, on the overall device performance. Moreover, the thermal stability and interface quality of the materials were assessed to address practical implementation challenges.

Among the tested electron transport layers (ETLs), WS_2 emerged as the most promising candidate, yielding superior results in key performance metrics. The optimized device structure achieved

a remarkable power conversion efficiency (PCE) of 33.43%, along with an open-circuit voltage (V_{oc}) of 1.104V, a short-circuit current density (J_{sc}) of 34.43 mA/cm², and a fill factor (FF) of 88.38%. These figures represent a significant improvement over existing lead-free PSC designs and demonstrate the potential of this architecture in high-efficiency photovoltaic applications.

Additionally, the study presents a comparative analysis with previously reported designs, highlighting the benefits of material selection and structural optimization. The favorable simulated outcomes suggest that this design could pave the way for the development of stable, flexible, and lead-free solar cells suitable for next-generation optoelectronic and wearable energy applications.

Overall, this work contributes valuable insights into the material engineering and structural tuning of eco-friendly PSCs, reinforcing the feasibility of sustainable and efficient solar technologies without compromising performance.

Funding Information:

No external funding was obtained for this work.

References

- [1] C. Liu, H. Mohammadpourkarbasi, and S. Sharples, "Life cycle carbon and cost assessments of the retrofit to Passivhaus EnerPHit standard of suburban residential buildings in Hunan, China," *Energy Build*, vol. 332, p. 115417, Apr. 2025, doi: 10.1016/j. enbuild.2025.115417.
- [2] Q. Hassan *et al.*, "The renewable energy role in the global energy Transformations," *Renewable Energy Focus*, vol. 48, p. 100545, Mar. 2024, doi: 10.1016/j.ref.2024.100545.
- [3] N. Kannan and D. Vakeesan, "Solar energy for future world: A review," Renewable and Sustainable Energy Reviews, vol. 62, pp. 1092–1105, Sep. 2016, doi: 10.1016/j.rser.2016.05.022.
- [4] F. M. Guangul and G. T. Chala, "Solar Energy as Renewable Energy Source: SWOT Analysis," in 2019 4th MEC International Conference on Big Data and Smart City (ICBDSC), IEEE, Jan. 2019, pp. 1–5. doi: 10.1109/ICBDSC.2019.8645580.

- [5] M. H. Ahmadi *et al.*, "Renewable energy harvesting with the application of nanotechnology: A review," *Int J Energy Res*, vol. 43, no. 4, pp. 1387–1410, Mar. 2019, doi: 10.1002/er.4282.
- [6] K. Ellmer, "Past achievements and future challenges in the development of optically transparent electrodes," *Nat Photonics*, vol. 6, no. 12, pp. 809–817, Dec. 2012, doi: 10.1038/nphoton.2012.282.
- [7] T. M. Clarke and J. R. Durrant, "Charge Photogeneration in Organic Solar Cells," *Chem Rev*, vol. 110, no. 11, pp. 6736–6767, Nov. 2010, doi: 10.1021/cr900271s.
- [8] F. Behrouznejad, S. Shahbazi, N. Taghavinia, H.-P. Wu, and E. Wei-Guang Diau, "A study on utilizing different metals as the back contact of CH 3 NH 3 PbI 3 perovskite solar cells," *J Mater Chem A Mater*, vol. 4, no. 35, pp. 13488–13498, 2016, doi: 10.1039/C6TA05938D.

- [9] J. Pastuszak and P. Węgierek, "Photovoltaic Cell Generations and Current Research Directions for Their Development," *Materials*, vol. 15, no. 16, p. 5542, Aug. 2022, doi: 10.3390/ma15165542.
- [10] P. Basumatary and P. Agarwal, "A short review on progress in perovskite solar cells," *Mater Res Bull*, vol. 149, p. 111700, May 2022, doi: 10.1016/j.materresbull.2021.111700.
- [11] M. Balat, "Solar Technological Progress and Use of Solar Energy in the World," Energy Sources, Part A: Recovery, Utilization, and Environmental Effects, vol. 28, no. 10, pp. 979–994, Jun. 2006, doi: 10.1080/009083190953409.
- [12] R. R. King *et al.*, "Solar cell generations over 40% efficiency," *Progress in Photovoltaics: Research and Applications*, vol. 20, no. 6, pp. 801–815, Sep. 2012, doi: 10.1002/pip.1255.
- [13] H. Zhang, X. Ji, H. Yao, Q. Fan, B. Yu, and J. Li, "Review on efficiency improvement effort of perovskite solar cell," *Solar Energy*, vol. 233, pp. 421–434, Feb. 2022, doi: 10.1016/j. solener.2022.01.060.
- [14] N. Suresh Kumar and K. Chandra Babu Naidu, "A review on perovskite solar cells (PSCs), materials and applications," *Journal of Materiomics*, vol. 7, no. 5, pp. 940–956, Sep. 2021, doi: 10.1016/j.jmat.2021.04.002.
- [15] M. H. Ahmadi *et al.*, "Renewable energy harvesting with the application of nanotechnology: A review," *Int J Energy Res*, vol. 43, no. 4, pp. 1387–1410, Mar. 2019, doi: 10.1002/er.4282.
- [16] D. B. Mitzi, S. Wang, C. A. Feild, C. A. Chess, and A. M. Guloy, "Conducting Layered Organic-inorganic Halides Containing \(\)110 \(\) -Oriented Perovskite Sheets," Science (1979), vol. 267, no. 5203, pp. 1473–1476, Mar. 1995, doi: 10.1126/science.267.5203.1473.
- [17] H. Arbouz, "Optimization of lead-free CsSnI 3 -based perovskite solar cell structure," *Applied Rheology*, vol. 33, no. 1, Feb. 2023, doi: 10.1515/arh-2022-0138.

- [18] N. Ali *et al.*, "A review on perovskite materials with solar cell prospective," *Int J Energy Res*, vol. 45, no. 14, pp. 19729–19745, Nov. 2021, doi: 10.1002/er.7067.
- [19] S. J. Adjogri and E. L. Meyer, "A Review on Lead-Free Hybrid Halide Perovskites as Light Absorbers for Photovoltaic Applications Based on Their Structural, Optical, and Morphological Properties," *Molecules*, vol. 25, no. 21, p. 5039, Oct. 2020, doi: 10.3390/molecules25215039.
- [20] Z. Li, W. Zhou, X. Zhang, Y. Gao, and S. Guo, "High-efficiency, flexibility and lead-free X-ray shielding multilayered polymer composites: layered structure design and shielding mechanism," *Sci Rep*, vol. 11, no. 1, p. 4384, Feb. 2021, doi: 10.1038/s41598-021-83031-4.
- [21] Md. F. Rahman *et al.*, "Design and numerical analysis of CIGS-based solar cell with V2O5 as the BSF layer to enhance photovoltaic performance," *AIP Adv*, vol. 13, no. 4, Apr. 2023, doi: 10.1063/5.0138354.
- [22] A. Isha *et al.*, "High efficiency Cu2MnSnS4 thin film solar cells with SnS BSF and CdS ETL layers: A numerical simulation," *Heliyon*, vol. 9, no. 5, p. e15716, May 2023, doi: 10.1016/j. heliyon.2023.e15716.
- [23] M. E. Islam, M. R. Islam, S. Ahmmed, M. K. Hossain, and M. F. Rahman, "Highly efficient SnS-based inverted planar heterojunction solar cell with ZnO ETL," *Phys Scr*, vol. 98, no. 6, p. 065501, Jun. 2023, doi: 10.1088/1402-4896/accb13.
- [24] K. Dris, M. Benhaliliba, A. Ayeshamariam, A. Roy, and K. Kaviyarasu, "Improving the perovskite solar cell by insertion of methyl ammonium tin oxide and cesium tin chloride as absorber layers: scaps 1d study based on experimental studies," *Journal of Optics*, Jul. 2024, doi: 10.1007/s12596-024-01996-7.
- [25] S. Mushtaq *et al.*, "Performance optimization of lead-free MASnBr3 based perovskite solar cells by SCAPS-1D device simulation," *Solar Energy*, vol. 249, 2023, doi: 10.1016/j. solener.2022.11.050.

- [26] S. Banik, A. Das, B. K. Das, and N. Islam, "Numerical simulation and performance optimization of a lead-free inorganic perovskite solar cell using SCAPS-1D," *Heliyon*, vol. 10, no. 1, 2024, doi: 10.1016/j.heliyon.2024. e23985.
- [27] B. Sultana, A. T. M. S. Islam, M. D. Haque, A. Kuddus, M. H. Ali, and M. F. Rahman, "Numerical study of MoSe2-based dual-heterojunction with In2Te3 BSF layer toward high-efficiency photovoltaics," *Phys Scr*, vol. 98, no. 9, 2023, doi: 10.1088/1402-4896/acee29.
- [28] K. Sobayel *et al.*, "A comprehensive defect study of tungsten disulfide (WS2) as electron transport layer in perovskite solar cells by numerical simulation," *Results Phys*, vol. 12, 2019, doi: 10.1016/j.rinp.2018.12.049.
- [29] Y. Gan *et al.*, "Numerical investigation energy conversion performance of tin-based perovskite solar cells using cell capacitance simulator," *Energies (Basel)*, vol. 13, no. 22, 2020, doi: 10.3390/en13225907.
- [30] T. A. Chowdhury, R. B. Arif, H. Israq, N. Sharmili, and R. S. Shuvo, "SCAPS numerical design of MoSe2 solar cell for different buffer layers," *Chalcogenide Letters*, vol. 21, no. 2, pp. 175–187, Mar. 2024, doi: 10.15251/CL.2024.212.175.
- [31] K. Deepthi Jayan and V. Sebastian, "Modelling and comparative performance analysis of tin based mixed halide perovskite solar cells with IGZO and CuO as charge transport layers," *Int J Energy Res*, vol. 45, no. 11, 2021, doi: 10.1002/er.6909.
- [32] A. Hima, "Enhancing of CH3NH3SnI3 based solar cell efficiency by ETL engineering," *International Journal of Energetica*, vol. 5, no. 1, 2020, doi: 10.47238/ijeca.v5i1.119.
- [33] N. Balaa and S. K. Mallik, "Comparative Study of Lead-free Perovskite Materials MASnI3, MASnBr3 and MAGeI3 to Design, Simulate and Optimize Lead Free PSC," *Indian Journal of Pure & Applied Physics*, vol. 64, no. 4, pp. 292–303, 2024, doi: 10.56042/ijpap.v62i4.7435.

- [34] M. K. Hossain *et al.*, "Deep Insights into the Coupled Optoelectronic and Photovoltaic Analysis of Lead-Free CsSnI 3 Perovskite-Based Solar Cell Using DFT Calculations and SCAPS-1D Simulations," *ACS Omega*, vol. 8, no. 25, pp. 22466–22485, Jun. 2023, doi: 10.1021/acsomega.3c00306.
- [35] A. I. Shimul, A. T. M. S. Islam, A. Ghosh, M. M. Hossain, S. A. Dipa, and R. J. Ramalingam, "Investigating charge transport layer flexibility for boosted performance in Lead-Free CsSnBr3-based perovskite solar cells," Comput Mater Sci, vol. 250, p. 113701, Feb. 2025, doi: 10.1016/j.commatsci.2025.113701.
- [36] Y. Raoui, H. Ez-Zahraouy, N. Tahiri, O. El Bounagui, S. Ahmad, and S. Kazim, "Performance analysis of MAPbI3 based perovskite solar cells employing diverse charge selective contacts: Simulation study," Solar Energy, vol. 193, pp. 948–955, Nov. 2019, doi: 10.1016/j.solener.2019.10.009.
- [37] O. Ahmad, A. Rashid, M. W. Ahmed, M. F. Nasir, and I. Qasim, "Performance evaluation of Au/p-CdTe/Cs2TiI6/n-TiO2/ITO solar cell using SCAPS-1D," *Opt Mater (Amst)*, vol. 117, p. 111105, Jul. 2021, doi: 10.1016/j.optmat.2021.111105.
- [38] A. Mohandes, M. Moradi, and H. Nadgaran, "Numerical simulation of inorganic Cs2AgBiBr6 as a lead-free perovskite using device simulation SCAPS-1D," Apr. 15, 2021. doi: 10.21203/rs.3.rs-320895/v1.
- [39] L. Lin, L. Jiang, P. Li, B. Fan, and Y. Qiu, "A modeled perovskite solar cell structure with a Cu2O hole-transporting layer enabling over 20% efficiency by low-cost low-temperature processing," *Journal of Physics and Chemistry of Solids*, vol. 124, pp. 205–211, Jan. 2019, doi: 10.1016/j.jpcs.2018.09.024.
- [40] T. Minemoto and M. Murata, "Device modeling of perovskite solar cells based on structural similarity with thin film inorganic semiconductor solar cells," *J Appl Phys*, vol. 116, no. 5, Aug. 2014, doi: 10.1063/1.4891982.

- [41] K. Amri, R. Belghouthi, R. Gharbi, and M. Aillerie, "Effect of defect densities and absorber thickness on carrier collection in Perovskite solar cells," in 2020 7th International Conference on Control, Decision and Information Technologies (CoDIT), IEEE, Jun. 2020, pp. 599-603. doi: 10.1109/CoDIT49905.2020.9263934.
- [42] M. S. Uddin *et al.*, "An In-Depth Investigation of the Combined Optoelectronic and Photovoltaic Properties of Lead-Free Cs 2 AgBiBr 6 Double Perovskite Solar Cells Using DFT and SCAPS-1D Frameworks," *Adv Electron Mater*, vol. 10, no. 5, May 2024, doi: 10.1002/aelm.202300751.
- [43] H.-J. Du, W.-C. Wang, and J.-Z. Zhu, "Device simulation of lead-free CH 3 NH 3 SnI 3 perovskite solar cells with high efficiency," *Chinese Physics B*, vol. 25, no. 10, p. 108802, Oct. 2016, doi: 10.1088/1674-1056/25/10/108802.
- [44] N. Lakhdar and A. Hima, "Electron transport material effect on performance of perovskite solar cells based on CH3NH3GeI3," *Opt Mater* (*Amst*), vol. 99, p. 109517, Jan. 2020, doi: 10.1016/j.optmat.2019.109517.
- [45] E. S. Hossain, P. Chelvanathan, S. A. Shahahmadi, K. Sopian, B. Bais, and N. Amin, "Performance assessment of Cu2SnS3 (CTS) based thin film solar cells by AMPS-1D," *Current Applied Physics*, vol. 18, no. 1, pp. 79–89, Jan. 2018, doi: 10.1016/j.cap.2017.10.009.
- [46] L. Lin *et al.*, "Simulated development and optimized performance of CsPbI3 based allinorganic perovskite solar cells," *Solar Energy*, vol. 198, pp. 454–460, Mar. 2020, doi: 10.1016/j. solener.2020.01.081.
- [47] A. I. Shimul, M. M. Hossain, and S. A. Dipa, "Investigating the effectiveness of Ca3AsCl3-based Perovskite Solar Cells with optimal hole transport layer selection through numerical optimization and machine learning," *Opt Commun*, vol. 586, p. 131916, Aug. 2025, doi: 10.1016/j.optcom.2025.131916.

- [48] A. I. Shimul, S. R. Sarker, M. M. Hossain, S. K. Ghosh, M. J. Naime, and S. A. Dipa, "Enhancing the Efficiency of (CH 3 NH 3) 2 CuCl 4-based Perovskite Solar Cells by Selecting a Suitable Electron Transport Layer," In 2025 International Conference on Electrical, Computer and Communication Engineering (ECCE), pp. 1–6, 2025.
- [49] S. R. Sarker, A. Islam Shimul, M. M. Hossain, Md. Eakub Ali, Md. N. Sadman, and S. Aktar Dipa, "Numerical Investigation of a Novel Lead-Free Perovskite Solar Cell with FTO/WS 2 /CsSnI 3 /NiO Architecture For High-Efficiency Photovoltaic Applications," in 2025 International Conference on Electrical, Computer and Communication Engineering (ECCE), IEEE, Feb. 2025, pp. 1–5. doi: 10.1109/ECCE64574.2025.11013974.
- [50] A. I. Shimul, S. R. Sarker, M. M. Hossain, S. Alam, A. Shahriare, and S. A. Dipa, "Numerical Optimization and High-Performance Design of Lead-Free CsSnBr 3 Perovskite Solar Cells with Optimal Hole Transport Layer Selection," in 2024 13th International Conference on Electrical and Computer Engineering (ICECE), IEEE, Dec. 2024, pp. 148–153. doi: 10.1109/ICECE64886.2024.11024714.
- [51] A. I. Shimul, A. T. M. S. Islam, A. Ghosh, M. M. Hossain, S. A. Dipa, and R. J. Ramalingam, "Investigating charge transport layer flexibility for boosted performance in Lead-Free CsSnBr3-based perovskite solar cells," Comput Mater Sci, vol. 250, p. 113701, Feb. 2025, doi: 10.1016/j.commatsci.2025.113701.
- [52] F.Oufqir, M. Bendaoud, F. E. Tahiri, and K. Chikh, "Advanced integration of a switched-coupled-inductor Ćuk converter for optimized grid-connected PV application," *Renewable Energy and Sustainable Development*, vol. 11, no. 1, p. 58, Feb. 2025, doi: 10.21622/resd.2025.11.1.1128.
- [53] P. Singh, N. K. Singh, and A. K. Singh, "Intelligent hybrid method to predict generated power of solar PV system," *Renewable Energy and Sustainable Development*, vol. 11, no. 1, p. 141, May 2025, doi: 10.21622/resd.2025.11.1.1264.

- [54] R. T. Moyo, M. Dewa, H. F. M. Romero, V. A. Gómez, J. I. M. Aragonés, and L. Hernández-Callejo, "An adaptive neuro-fuzzy inference scheme for defect detection and classification of solar PV cells," Renewable Energy and Sustainable Development, vol. 10, no. 2, p. 218, Sep. 2024, doi: 10.21622/resd.2024.10.2.929.
- [55] S. Bouafia and M. Si Abdallah, "Numerical study of a solar PV/thermal collector under several conditions in Algeria," *Renewable Energy and Sustainable Development*, vol. 10, no. 2, p. 233, Sep. 2024, doi: 10.21622/resd.2024.10.2.900.
- [56] A.-M. Y. Yidana, "2d solar thermal direct absorption comparison between gold and silver nanoparticle," *Renewable Energy and Sustainable Development*, vol. 9, no. 2, p. 32, Oct. 2023, doi: 10.21622/resd.2023.09.2.032.
- [57] S. S. Jaafar, H. A. Maarof, R. T. Salh, H. Sahib, and Y. H. Azeez, "Non-uniform dust distribution effect on photovoltaic panel performance," Renewable Energy and Sustainable Development, vol. 9, no. 1, p. 01, Feb. 2023, doi: 10.21622/resd.2023.09.1.001.
- [58] A. Bag, R. Radhakrishnan, R. Nekovei, and R. Jeyakumar, "Effect of absorber layer, hole transport layer thicknesses, and its doping density on the performance of perovskite solar cells by device simulation," Solar Energy, vol. 196, 2020, doi: 10.1016/j.solener.2019.12.014.
- [59] P. K. Patel, "Device simulation of highly efficient eco-friendly CH3NH3SnI3 perovskite solar cell," *Sci Rep*, vol. 11, no. 1, p. 3082, Feb. 2021, doi: 10.1038/s41598-021-82817-w.
- [60] M. M. Otrokov et al., "Evidence of large spinorbit coupling effects in quasi-free-standing graphene on Pb/Ir(111)," 2d Mater, vol. 5, no. 3, p. 035029, Jun. 2018, doi: 10.1088/2053-1583/ aac596.
- [61] W. Ahmad, M. Noman, S. Tariq Jan, and A. D. Khan, "Performance analysis and optimization of inverted inorganic CsGeI 3 perovskite cells with carbon/copper charge transport materials using SCAPS-1D," R Soc Open Sci, vol. 10, no. 3, Mar. 2023, doi: 10.1098/ rsos.221127.

- [62] H. Zhou *et al.*, "Interface engineering of highly efficient perovskite solar cells," *Science* (1979), vol. 345, no. 6196, pp. 542–546, Aug. 2014, doi: 10.1126/science.1254050.
- [63] S. A. Dar and B. S. Sengar, "Optimization and Performance Analysis of Inorganic Lead-Free CsSnBr3 Perovskite Solar Cells Using Diverse Electron Transport Materials," *Energy & Fuels*, vol. 38, no. 9, pp. 8229–8248, 2024.
- [64] A. Gheno, T. T. Thu Pham, C. Di Bin, J. Bouclé, B. Ratier, and S. Vedraine, "Printable WO3 electron transporting layer for perovskite solar cells: Influence on device performance and stability," Solar Energy Materials and Solar Cells, vol. 161, pp. 347–354, Mar. 2017, doi: 10.1016/j.solmat.2016.10.002.
- [65] O. Ahmad, A. Rashid, M. W. Ahmed, M. F. Nasir, and I. Qasim, "Performance evaluation of Au/ p-CdTe/Cs2TiI6/n-TiO2/ITO solar cell using SCAPS-1D," Opt Mater (Amst), vol. 117, p. 111105, Jul. 2021, doi: 10.1016/j.optmat.2021.111105.
- [66] A. Mohandes, M. Moradi, and H. Nadgaran, "Numerical simulation of inorganic Cs2AgBiBr6 as a lead-free perovskite using device simulation SCAPS-1D," *Opt Quantum Electron*, vol. 53, no. 6, p. 319, Jun. 2021, doi: 10.1007/s11082-021-02959-z.
- [67] L. Lin, L. Jiang, P. Li, B. Fan, and Y. Qiu, "A modeled perovskite solar cell structure with a Cu2O hole-transporting layer enabling over 20% efficiency by low-cost low-temperature processing," Journal of Physics and Chemistry of Solids, vol. 124, pp. 205–211, Jan. 2019, doi: 10.1016/j.jpcs.2018.09.024.
- [68] T. Minemoto and M. Murata, "Device modeling of perovskite solar cells based on structural similarity with thin film inorganic semiconductor solar cells," J Appl Phys, vol. 116, no. 5, Aug. 2014, doi: 10.1063/1.4891982.
- [69] K. Amri, R. Belghouthi, R. Gharbi, and M. Aillerie, "Effect of defect densities and absorber thickness on carrier collection in Perovskite solar cells," in 2020 7th International Conference on Control, Decision and Information Technologies (CoDIT), IEEE, Jun. 2020, pp. 599–603. doi: 10.1109/CoDIT49905.2020.9263934.